symmetry

MDPI

Article

Energy Efficiency Enhanced Landing Strategy for Manned eVTOLs Using L_1 Adaptive Control

Zian Wang [1,*,†], Shengchen Mao [1,†], Zheng Gong [1,*], Chi Zhang [2] and Jun He [3]

[1] School of Aerospace Engineering, Nanjing University of Aeronautics and Astronautics, Nanjing 210016, China; maoshengchen@nuaa.edu.cn
[2] COMAC Beijing Aircraft Technology Research Institute, Beijing 100083, China; zhang-c20@mails.tsinghua.edu.cn
[3] School of Aerospace Engineering, Shenyang Aerospace University, Shenyang 110136, China; 13840342646@139.com
* Correspondence: wangzian@nuaa.edu.cn (Z.W.); matthewzhenggong@nuaa.edu.cn (Z.G.)
† These authors contributed equally to this work and should be considered co-first authors.

Abstract: A new landing strategy is presented for manned electric vertical takeoff and landing (eVTOL) vehicles, using a roll maneuver to obtain a trajectory in the horizontal plane. This strategy rejects the altitude surging in the landing process, which is the fatal drawback of the conventional jumping strategy. The strategy leads to a smoother transition from the wing-borne mode to the thrust-borne mode, and has a higher energy efficiency, meaning a better flight experience and higher economic performance. To employ the strategy, a five-stage maneuver is designed, using the lateral maneuver instead of longitudinal climbing. Additionally, a control system based on L_1 adaptive control theory is designed to assist manned driving or execute flight missions independently, consisting of the guidance logic, stability augmentation system and flight management unit. The strategy is verified with the ET120 platform, by Monte Carlo simulation for robustness and safety performance, and an experiment was performed to compare the benefits with conventional landing strategies. The results show that the performance of the control system is robust enough to reduce perturbation by at least 20% in all modeling parameters, and ensures consistent dynamic characteristics between different flight modes. Additionally, the strategy successfully avoids climbing during the landing process with a smooth trajectory, and reduces the energy consumed for landing by 64%.

Keywords: eVTOL; flight dynamics modeling; L_1 adaptive control; guidance; deceleration and landing strategy; energy efficiency; Monte Carlo simulation

Citation: Wang, Z.; Mao, S.; Gong, Z.; Zhang, C.; He, J. Energy Efficiency Enhanced Landing Strategy for Manned eVTOLs Using L_1 Adaptive Control. *Symmetry* **2021**, *13*, 2125. https://doi.org/10.3390/sym13112125

Academic Editors: Chengxi Zhang, Jin Wu and Chong Li

Received: 3 October 2021
Accepted: 21 October 2021
Published: 8 November 2021

1. Introduction

Electric vertical takeoff and landing (eVTOL) vehicles are an emerging class of aircraft configurations. This configuration highlights the distributed propulsion (DEP) system, which enables vehicles to cruise economically and take off and land vertically by switching between the fixed-wing mode and a multi-rotor mode. According to Ref. [1], DEP gives the vehicle the potential to be more efficient, flexible and reliable than conventional VTOLs, by changing the flight mode from thrust-borne flight to wing-borne flight. This in turn changes the dynamic characteristics of the flight significantly, and poses challenges with respect to the design of strategies and control laws to ensure uniform flight in the entire envelope [2]. The existing studies pay much attention to the takeoff and acceleration phase and cruise trajectory scheduling, but little attention has been paid to deceleration and landing strategies [3].

The existing landing strategies are insufficient for manned eVTOL vehicles [4–6]. The conventional landing strategy, which causes the vehicle to jump steeply, results in a poor comfort level, due to the high degree of normal overload and the rapid change in pressure with altitude, as well as low efficiency, because most of the kinetic energy is not dissipated,

but rather converted into gravity potential energy, resulting in considerable time and rotor energy wasted in the subsequent vertical landing phase. The post-stall maneuver strategy is highly efficient for unmanned aerial vehicles (UAVs), because the angle of attack is pulled up into the stall region, meaning there is no excessive lift generated in order to rise, and greater drag coefficients for a produced for the energy to dissipate. However, a fatal defect of this strategy is that it is highly possible for the vehicles to go out of control in the stall region [7], which is unacceptable for manned air service.

The fact that the eVTOL aircraft possesses symmetry in the lateral channels prompted us to design a landing strategy making the most of these lateral symmetry characteristics. The landing procedure is conducted in a three-dimensional (3D) environment, while the aforementioned strategies all plan a two-dimensional (2D) trajectory [8]. Ref. [9] proposes a rolling-horizon landing arrival scheduling method for eVTOLs from the perspective of the management of limited vertiports in peak hours. This prompted us to design a deceleration and landing strategy that can take advantage of the vast 3D airspace around the vertiports, avoiding this abrupt, altitude-increasing maneuver. The symmetrical characteristics in the roll control channels makes the strategy more feasible in real-world application [10].

Usually, a strategy is performed with the assistance of control systems, especially for vehicles with complicated dynamic characteristics [11–15]. The conventional Proportional-Integral-Derivative control systems are widely used in normal fixed-wing aircrafts, but are seldom used for advanced configured flights, due to their limited robustness performance and the vast flight envelope of the advanced vehicles [16]. Artificial neural network systems with model predictive control are able to adapt to the variations in the dynamics of the plants [17,18]. However, the long iteration cycles and computational time are fatal, as change in flight mode is a rapid process. The model-based control theories, namely, the nonlinear dynamic inversion (NDI) and the quantitative feedback theory, are rapid enough and can ensure precise tracking, but they strongly rely on model precision, which is unrealistic for new configurations [19,20]. Aircrafts with vertical takeoff and landing abilities usually require customized control systems that can adapt to changes in control strategies and dynamic characteristics, and can provide sufficient robustness margins and fault tolerance [21–25]. Targeted at the multiple flight modes and the modeling uncertainties of eVTOLs, a control system implemented with L_1 controllers is designed.

The L_1 adaptive control algorithm is sufficiently fast and robust to be equipped on a flight control system for eVTOLs. This algorithm has been applied in various plants successfully, including in aerospace, nuclear technics, marine, etc., contexts [26,27]. The basic principle of the L_1 adaptive theory is the use of a low-pass filter to purify the model error of fast-varying external disturbances, thus decoupling the adaptive performance from the robustness performance [28,29]. Its successful application in multiple flight tests has convinced aerospace engineers of its ability to reject rapidly varying uncertainties, significantly changing the plant dynamics [12,30]. Additionally, controllers based on L_1 theory avoid complicated and time-consuming gain-scheduling, making the control system more customer-friendly [12,31]. With the assistance of the L_1 control system, pilots can perform the strategy at a low level of work load, because the autopilot is able to plan the landing trajectory and make the vehicle track it using the guidance logic, while the stability augmentation system ensures consistent flight performance in all flight modes. The details of the strategy and assistance control system are presented in this paper. The main contents of this work are as follows:

1. Flight dynamics modeling of a large-scale 120 kg electric-vertical takeoff and landing vehicle (ET120), and an analysis of the dynamic characteristics of the system.
2. The design of a four-layer control system based on the L_1 adaptive controller for baseline angular rate control, and a stability analysis of the controller.
3. The design of a roll-horizon deceleration and vertical landing strategy that avoids altitude surging using a smooth transition from fixed-wing mode to multi-rotor mode, along with the maneuver and guidance logic.

4. Monte Carlo simulations for controller performance and strategy performance verification and parameter setting. Comparison simulations with the conventional strategy are performed for validation.

2. Platform Modeling and Dynamics Analysis

2.1. Platform Introduction

The study object of this work was the ET120 platform (as shown in Figure 1), a laterally symmetric eVTOL configuration developed for future urban air mobility. The main body of the platform is a lifting body consistent with normal fixed-wing configurations, consisting of the fuselage, wings and T-tails. The DEP system distinguishes the ET120 from conventional aircraft, where four pairs of vertically mounted rotors provide the hovering power, and one horizontally mounted rotor provides the propulsion power. The geometric parameters of the protype ET120 are given in Table 1.

Table 1. The geometric parameters of ET120.

Parameters	Values
Reference area (m^2)	3.0103
Wing span (m)	5.8
Mean aerodynamic chord (m)	0.6
Mass (kg)	120

The DEP system, together with the aerodynamic surfaces, engages in the flight control in different ways, according to the flight mode. In fixed-wing mode, the attitude control is practiced by the deflection aerodynamic control surfaces. Namely, the aileron deflection δ_a, elevator deflection δ_e and the rudder deflection δ_r. The velocity is controlled by the speed of the propulsion rotor δ_t. In multi-rotor mode, the attitudes are controlled by the speed difference of the hovering rotors, n_ϕ, n_θ and n_φ. The altitude controllable variable is the total speed of the hovering rotors n_h. The flight speed is controlled by the attitude, given the total hovering rotor speed, which makes the vehicle an under-actuated system in multi-rotor mode. The physical control principles are illustrated in Table 2.

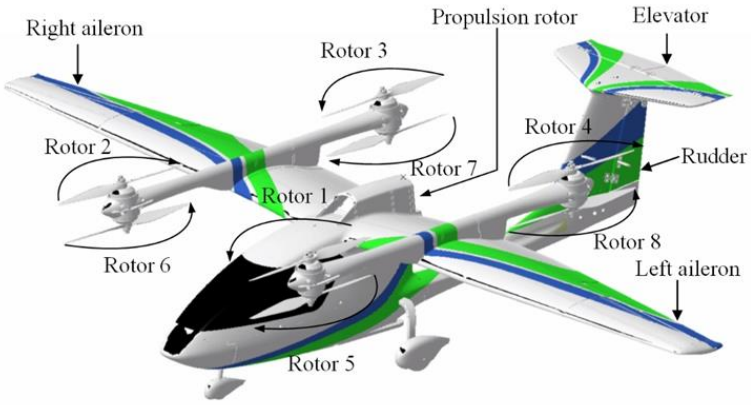

Figure 1. The actuators of the ET120 platform.

Table 2. The control methods of the ET120 in different modes.

Mode	Multi-Rotors	Transitional	Fixed-Wing
Roll	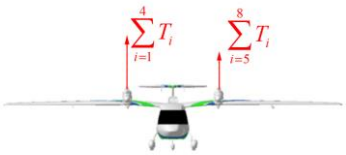	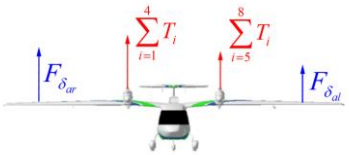	
Pitch	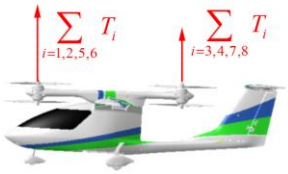		
Yaw	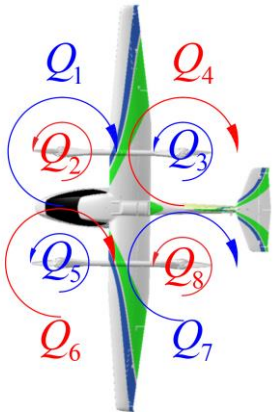	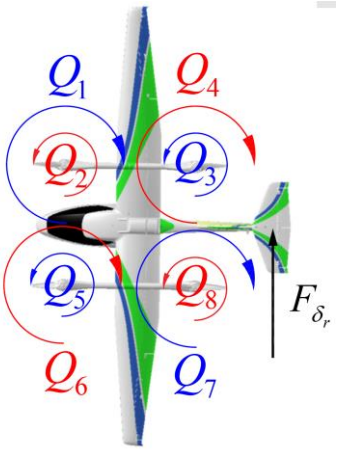	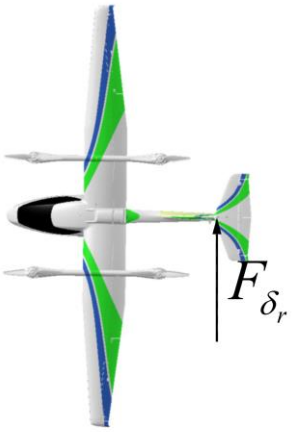
Vertical		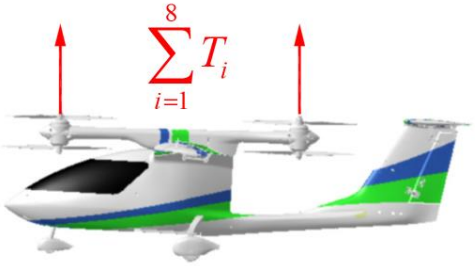	

2.2. Flight Dynamics Model

The dynamics model of ET120 is established based on the actual aircraft parameters and wind tunnel tests and are separated into 3 main parts:

The mass balance part. This part gives the gravity and the position of its center.

The aerodynamics part. This part concerns the pure aerodynamic forces and moments provided by the fixed-wing part, including the fuselage, the wings, the tails and the aero-surfaces. High-quality aerodynamics data are obtained from wind tunnel tests.

The propulsion system part. This part provides the forces and moments produced by each rotor. The thrust and torque and tilt moments at different inflow velocity and inflow angles are obtained using the blade element momentum theory (BEMT) mentioned in Ref. [7].

The forces and moments given by the above three parts are added up and projected to the body frame, outputting the overall force vector $\boldsymbol{F} = \begin{bmatrix} F_x & F_y & F_z \end{bmatrix}^T$ and moment vector $\boldsymbol{M} = \begin{bmatrix} L & M & N \end{bmatrix}^T$. Then the 6 DOF function of the ET120 can be modeled as:

$$\dot{\boldsymbol{V}} = \frac{\boldsymbol{F}}{m} - \boldsymbol{\Omega} \times \boldsymbol{V} \tag{1}$$

$$\dot{\boldsymbol{\Omega}} = \boldsymbol{J}^{-1}[\boldsymbol{M} - \boldsymbol{\Omega} \times (\boldsymbol{J} \cdot \boldsymbol{\Omega})] \tag{2}$$

$$\dot{\boldsymbol{\theta}} = \boldsymbol{E}\boldsymbol{\Omega} \tag{3}$$

$$\dot{\boldsymbol{I}} = \boldsymbol{R}_b^e \boldsymbol{V} \tag{4}$$

where $\boldsymbol{V} = [u, v, w]^T$ is the velocity vector in the body frame; m is the mass property; $\boldsymbol{\theta} = [\phi, \theta, \varphi]^T$ are Euler angles, with ϕ, θ and φ being the roll, pitch and yaw, respectively; $\boldsymbol{\Omega} = [p, q, r]^T$ are the angular rate in the body frame, with p, q and r being the roll, pitch, yaw angular rate, respectively; $\boldsymbol{I}$ is the position vector in earth frame, $\boldsymbol{J}$ is the inertia matrix, and $\boldsymbol{E}$ and $\boldsymbol{R}_b^e$ are the transform matrix from the angular vector to the Euler angular vector, and the rotation matrix from the body frame to the inertia frame, respectively.

2.3. Dynamics Anaylsis

The dynamics analysis is based on the trimming point of the ET120, using the linearized model of the flight dynamics model Equations (1)–(4). Due to the discrepancy in control actuators in different flight modes, the flight dynamic characteristics of the ET120 differ significantly. This consequently influences the control methods and control system design. The dynamic characteristics are reflected by the eigenvalue of the system matrix of the linearized model.

- Longitudinal

The longitudinal eigenvalues in different flight modes are depicted in Figure 2. The trimming states of these modes are set at:

1. Fixed-wing mode: airspeed (20 m/s~50 m/s), level flight.
2. Transitional mode: airspeed (2 m/s~20 m/s), level flight.
3. Multi-rotor mode: pitch angle (0~10°), hovering (airspeed zero).

In fixed-wing mode, the longitudinal eigenvalues are all complex numbers distributed on the left side of the coordinate planes, indicating oscillatory convergence with static stability. In transitional and hovering mode, the eigenvalues are two complex values with a negative real part and two complex values with a positive real part. This indicates static instability in longitudinal modes.

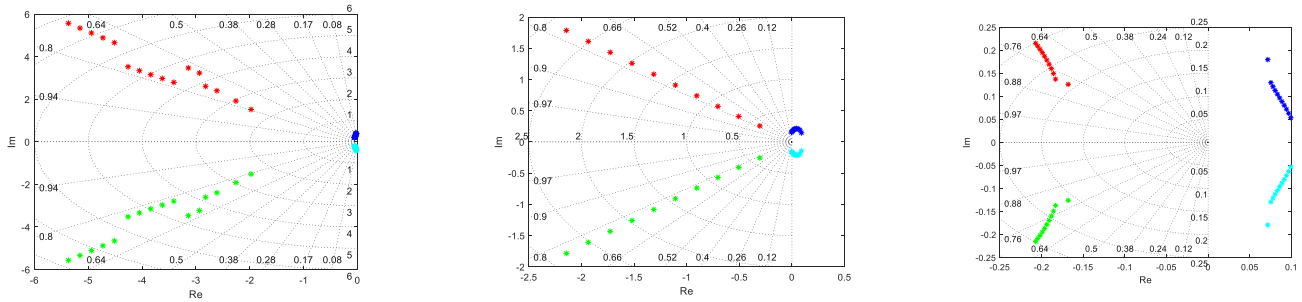

(**a**) (**b**) (**c**)

Figure 2. The longitudinal eigenvalues of the ET120 in different flight modes. (**a**) fixed-wing mode; (**b**) transitional mode; (**c**) multi-rotor mode.

- Lateral

The lateral eigenvalues are depicted in Figure 3. The trimming states of different flight modes are set as in the longitudinal analysis.

In fixed-wing mode and transitional mode, the eigenvalues are two conjugate complex numbers with negative real parts and a negative number and a positive number. This is consistent with normal fixed-wing vehicles, presenting an oscillatory converged Dutch roll mode, a converged roll mode and a slowly diverged spiral mode. However, in multi-rotor mode at low airspeed, the Dutch roll eigenvalues cross the imaginary axis. This indicates an abrupt change in the lateral dynamic characteristics in hovering mode.

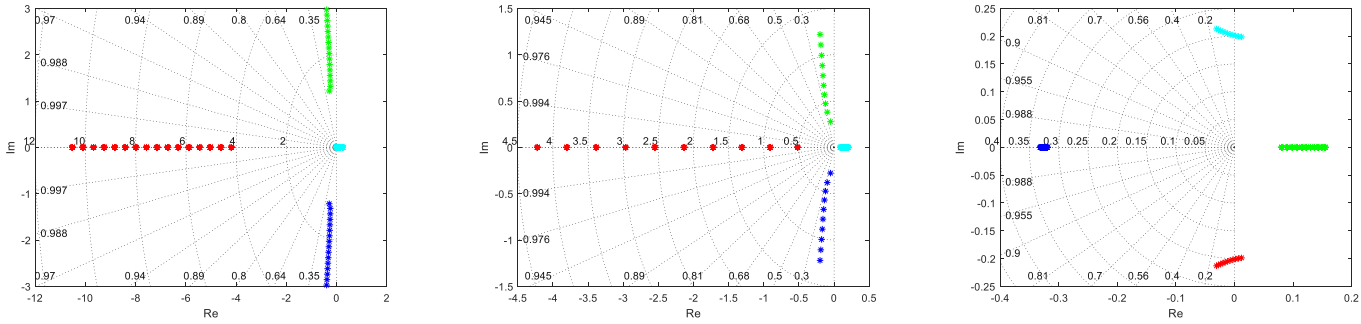

(**a**) (**b**) (**c**)

Figure 3. The lateral eigenvalues of the ET120 in different flight modes. (**a**) fixed-wing mode; (**b**) transitional mode; (**c**) multi-rotor mode.

- Numerical results

The numerical results for the dynamics analysis are given in Table 3. Clearly, the dynamic characteristics varies significantly both in longitudinal and lateral channels between the three flight modes. This feature of the ET120 prompted us to employ the L_1 adaptive control theory to address the model uncertainties and the dynamic characteristic changes during an entire envelope flight.

Table 3. The dynamic characteristics of the ET120.

	Channels		**Fixed-Wing**	**Transition**	**Multi-Rotor**
Longitudinal	Long-term	Frequency	0.39~0.41	diverged	diverged
		Damping ratio	0.042~0.306	diverged	diverged
	Short-term	Frequency	2.4~7.73	0.3982~2.78	0.21~0.298
		Damping ratio	0.672~0.79	0.766~0.768	0.6936~0.8
Lateral	Roll	Time constant	0.095~0.24	0.23~1.92	3.08~3.13
	Spiral	Time constant	−40~−130	−5.063~−11.23	−6.49~−11.56
	Dutch roll	Frequency	1.25~3.0	0.2816~1.23	cross imaginary axis
		Damping ratio	0.133~0.234	0.1619~0.1794	cross imaginary axis

3. Control System Design

As shown in Figure 4, a four-layer flight control system is designed for the ET120, including: a trajectory planner, a flight management unit, a guidance layer, and a control stability augmentation layer. The trajectory planner generates the flight path with navigation information. The flight management unit decides the navigation and control modes of the vehicle, e.g., the waypoint mode for navigation, the fixed-wing mode for flight control. The guidance layer drives the ET120 to follow the path at the desired airspeed, according to the chosen flight mode management unit. The control stability augmentation

layer is used to enhance control stability in both rotor and fixed-wing modes. By using the single-input–single-output (SISO) structure, the guidance and control algorithms in the longitudinal, lateral, and directional channels are designed independently. As this work focuses on strategy design, this section only discusses the inner loop control stability augmentation, and the guidance logic is discussed with respect to the maneuver strategy design, while the other layers are omitted.

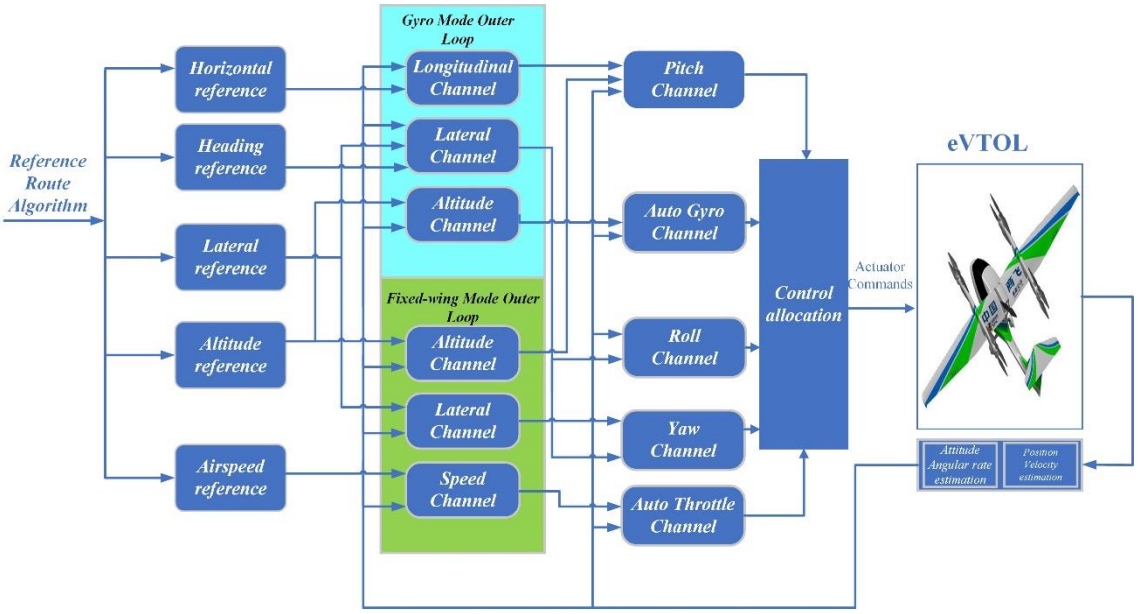

Figure 4. The control architecture of ET120.

3.1. Control Law

A three-axis stability augmentation system (CSAS) is designed to generate virtual angular acceleration commands and moment instructions to the control allocator. The baseline angular rate control, which is the basis of the whole control strategy, is practiced by this system. The CSAS is designed based on L_1 adaptive theory, which stands out in the following respects, compared to the conventional PID controller: (1) The performance of the L_1 controller relies less on model precision. (2) The L_1 controller avoids complicated gain scheduling. (3) It is easier for the L_1 controller to ensure level 1 flight quality, even though the plant is not ascertained. (4) In-time adjustment during flight is accessible to the L_1 controller. For slow loop control, namely, the pitch angle and the bank angle loop, an NDI controller is enough to provide the desired dynamic characteristics. As shown in Figure 5, the pitch and roll cascade channel naturally decouple the rapid angular rate control and slow attitude angle control according to the time-separation principle, where q_c, p_c and r_c are the pitch, roll and yaw rate command, respectively, and θ_c and ϕ_c are the pitch and roll commands, respectively. Owing to the similar control structures of the roll, pitch, and yaw channels, only the pitch channel is discussed here.

3.1.1. The Attitude NDI Controller

Based on the 6DOF function of the ET120, (2), (3), the control plant can be described as:

$$\dot{\theta}(t) = f_1(\theta(t), t) + g_1(\theta(t), t)q(t) \tag{5}$$

where $f_1(\theta(t), t)$, $g_1(\theta(t), t)$ are affine functions with $f_1(\theta(0), 0) = 0$ and $g_1(\theta(0), 0) = 1$.

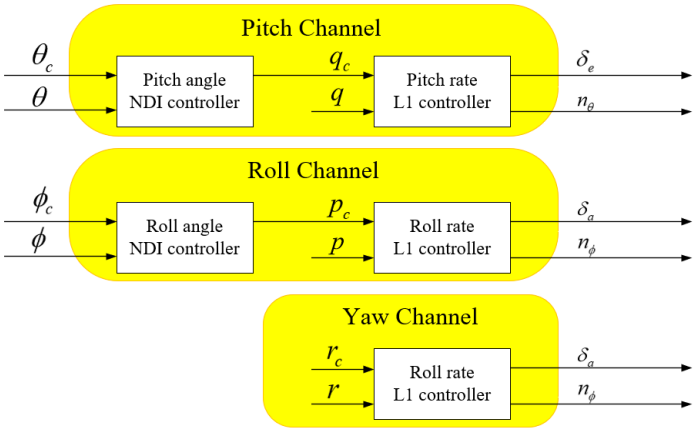

Figure 5. Three-axis decoupled control channels.

The tracking error $\Delta\theta(t)$ is the difference between the pitch angle command $\theta_c(t)$ and the actual pitch angle response $\theta(t)$, that is

$$\Delta\theta(t) = \theta_c(t) - \theta(t) \tag{6}$$

The NDI controller is designed as:

$$q_c(t) = g_1^{-1}(K_\theta \Delta\theta(t) - f_1(\theta(t), t)) \tag{7}$$

where the K_θ is the gain of the pitch angle.

3.1.2. The Angular Rate L_1 Controller

The L_1 controller is composed of four parts: the control plant, the control law, the state predictor and the adaptive law, which will be explained in this section.

- Control plant

The pitching rate function is derived from the 6DOF function (2); with the perturbation assumption, the system can be constructed by first-order coefficients M_α, M_q and $M_{\dot{q}_{vc}}$:

$$\dot{q}(t) = M_\alpha \alpha(t) + M_q q(t) + M_{\dot{q}_{vc}} \dot{q}_{vc}(t) \tag{8}$$

where $\dot{q}_{vc}(t)$ is the total virtual pitch angular acceleration. By moving the $\dot{q}_{vc}(t)$ term to the left and all the other terms to the right, we get:

$$\dot{q}_{vc}(t) = \frac{1}{M_{\dot{q}_{vc}}}[\dot{q}_c(t) - M_\alpha \alpha(t) - M_q q(t)] \tag{9}$$

Physically, the above function means the pitch acceleration is provided by the moments, and the right terms are generated by the aero-surfaces and the rotor system. If we define $\dot{q}_{ac}(t)$ to represent the angular acceleration provided by the aero-surfaces and $\dot{q}_{rc}(t)$ the rotor system, Equation (9) can be rewritten as:

$$\dot{q}_{vc}(t) = \dot{q}_{rc}(t) + \dot{q}_{ac}(t) \tag{10}$$

In hovering mode, the efficiency of the aero-surfaces is limited due to the low airspeed, and the majority of the control energy is generated by the hovering rotor system. It is reasonable that $\dot{q}_{vc}(t) \triangleq \dot{q}_{rc}(t)$, $\dot{q}_{ac}(t) \triangleq 0$. In fixed-wing mode, the hovering rotor is inactivated, and the situation is reversed, that is, $\dot{q}_{rc}(t) \triangleq 0$, $\dot{q}_{vc}(t) \triangleq \dot{q}_{ac}(t)$. During transition flight, both the aero-surfaces and hovering rotors achieve the commanded pitch angular acceleration.

Considering the modeling uncertainty, Equation (8) is rewritten as:

$$\dot{q}(t) = (M_\alpha + \hat{M}_\alpha)\alpha(t) + (M_q + \hat{M}_q)q(t) + (M_{\dot{q}_{vc}} + \hat{M}_{\dot{q}_{vc}})\dot{q}_{vc}(t) + \sigma_1 \tag{11}$$

where $\hat{M}_\alpha$, $\hat{M}_q$ and $\hat{M}_{\dot{q}_{vc}}$ are the coefficient uncertainties, and σ_1 is the disturbance factor. Substituting Equation (9) into Equation (10), we get:

$$\dot{q}(t) = \hat{M}_\alpha\alpha(t) + \hat{M}_q q(t) + \frac{\hat{M}_{\dot{q}_{vc}}}{M_{\dot{q}_{vc}}}(\dot{q}_c(t) - M_\alpha\alpha(t) - M_q q(t)) + \dot{q}_c(t) + \sigma_1 \tag{12}$$

With Equation (12), the first-order reference model can be constructed as follows:

$$\dot{q}(t) = -K_q q(t) + K_q q_c(t) \tag{13}$$

By combining Equations (12) and (13), we can rewrite the control plant of the pitch channel as:

$$\begin{cases} \dot{q}(t) = -K_q q(t) + K_q \eta(t) \\ \eta(t) = \omega_q \dot{q}_c(t) + f_2(t, q(t)) \\ f_2(t, q(t)) = \theta_q q(t) + \sigma_q \end{cases} \tag{14}$$

where $\omega_q = 1 + \frac{\hat{M}_{\dot{q}_{uc}}}{M_{\dot{q}_{uc}}}$ is the virtual control coefficient, $\theta_q = K_q - \frac{\hat{M}_{\dot{q}_{uc}}}{M_{\dot{q}_{uc}}} M_q$ is aerodynamic coefficient, and $\sigma_q = -\frac{\hat{M}_{\dot{q}_{uc}}}{M_{\dot{q}_{uc}}} M_\alpha \alpha + \sigma_1$ is the aerodynamic disturbance.

- The L_1 controller

The L_1 controller is designed based on the following assumptions, which can be measured in practical application.

Assumption 1. *The plant unknown coefficient ω_q is uniformly bounded in $[\omega_{ql}, \omega_{qu}]$, where ω_{ql} and ω_{qu} are the lower and upper bounds of ω_q.*

Assumption 2. *$f_2(t, 0)$ in Equation (14) is uniformly bounded, that is $\|f_2(t, 0)\|_\infty \leq b$, with $b > 0$, where $\|\bullet\|_\infty$ is the ∞-norm.*

Assumption 3. *The partial derivative of f_2 is semi-globally uniformly bounded: for each $\delta > 0$, there exists $d_{fq}(\delta) > 0$ and $d_{ft}(\delta) > 0$ that ensures the partial derivative of $f_2(t, q(t))$ is piecewise continuous regardless of time, which is written as:*

$$\begin{cases} \left\| \frac{\partial f_2(t, q(t))}{\partial q} \right\|_\infty \leq d_{\mathrm{f}q}(\delta), \\ \left\| \frac{\partial f_2(t, q(t))}{\partial t} \right\|_\infty \leq d_{\mathrm{ft}}(\delta). \end{cases} \tag{15}$$

For the inner loop control system, the uncertainty possesses a certain magnitude and limit, and these can be realized using engineering measures. These assumptions are easily satisfied in practical applications. Given these assumptions, the L_1 controller, which includes a state predictor, the adaptive law and the control law, can be designed with lemma 1:

Lemma 1. *For each $\tau \geq 0$, if $\|q_\tau\|_{L_\infty} \leq \rho$ and $\|\dot{q}_\tau\|_{L_\infty} \leq d$, where ρ and d are positive constants, and $\theta_q(t)$ and $\sigma_q(t)$ are continuous [29]. In addition, their derivatives for $t \in [0, \tau]$ are*

$$f(t, q(t)) = \theta_q(t)\|q_t\|_{L_\infty} + \sigma_q(t) \tag{16}$$

$$\left|\theta_q(t)\right| < d_{\mathrm{f}q}(\rho), \left|\dot{\theta}_q(t)\right| \leq d_\theta \tag{17}$$

$$\left|\sigma_q(t)\right| < b, \left|\dot{\sigma}_q(t)\right| \leq d_\sigma \tag{18}$$

where d_θ and d_σ are calculable limits; $\|\bullet\|_{L_\infty}$ is the L_∞-norm.

- State predictor

The state predictor is a system that reflects the control plants, and which has similar dynamic characteristics to the control plant. According to Equation (14), the state predictor can be designed as:

$$\begin{cases} \dot{\hat{q}}(t) = -K_q\hat{q}(t) + K_q\hat{\eta}(t) \\ \hat{\eta}(t) = \hat{\omega}_q(t)\dot{q}_c(t) + \hat{\theta}_q(t)q(t) + \hat{\sigma}_q(t) \\ \hat{y}(t) = \hat{q}(t) \end{cases} \tag{19}$$

where $\hat{\omega}_q(t)$ is the estimated uncertainty of the control factor, $\hat{\theta}_q(t)$ is the estimated uncertainty of the aerodynamic factor, and $\hat{\sigma}_q(t)$ is the estimated uncertainty of aerodynamic disturbance.

- Adaptive law

The adaptive gains are produced by:

$$\begin{cases} \dot{\hat{\theta}}_q(t) = \Gamma K_{proj}(\hat{\theta}_q(t), -\tilde{q}(t)PK_q\|q(t)\|_\infty) \\ \dot{\hat{\sigma}}_q(t) = \Gamma K_{proj}(\hat{\sigma}_q(t), -\tilde{q}(t)PK_q) \\ \dot{\hat{\omega}}_q(t) = \Gamma K_{proj}(\hat{\omega}_q(t), -\tilde{q}(t)PK_q\dot{q}_c(t)) \end{cases} \tag{20}$$

where Γ is adaptive gain, $\tilde{q}(t) = \hat{q}(t) - q(t)$ is tracking error, P is the solution of the Lyapunov equation $-K_q^T P - PK_q = -Q$, $Q > 0$. K_{proj} is the projection operator that can guarantee the boundedness of the adaptive parameters.

- Control law

The control law is given as:

$$\begin{cases} \dot{q}_c = K_d D[K_g q(t) - \hat{\omega}_q(t)\dot{q}_c(t) - \hat{\theta}_q(t)q(t) - \hat{\sigma}_q(t)] \\ \dot{q}_{vc} = \frac{1}{M_{\dot{q}_{vc}}}[\dot{q}_c - M_\alpha\alpha(t) - M_q q(t)] \end{cases} \tag{21}$$

where K_g is adaptive feedback gain, D is a low-pass filter and K_d is the adaptive feed forward gain, as depicted in Figure 6. The filter is expected to have dynamic characteristics that satisfy the following transfer function:

$$C(s) = \omega_q K_d D(s)(I + \omega_q K_d D(s))^{-1}, C(0) = I \tag{22}$$

where I is the identity matrix.

Additionally, the values of K_d and D should ensure that for a given ρ_0, there exists $\rho_r > \rho_{in}$ to maintain the L_1 norm condition:

$$\|G(s)\|_{L_1} < \frac{\rho_r - \|H(s)C(s)K_g\|_{L_1}\|q_c\|_{L_\infty} - \rho_{in}}{L_{\rho_r}\rho_r + b} \tag{23}$$

where $\|\bullet\|_{L_1}$ is the L_1-norm, and

$$\begin{cases} \rho_{in} := \|s(sI + K_q)^{-1}\|_{L_1}\rho_0 \\ H(s) = (sI + K_q)^{-1}K_q \\ G(s) = H(s)[I - C(s)] \\ L_{\rho_r} = \frac{\rho_r + \overline{\gamma}_1}{\rho_r} d_{\mathrm{fq}}[\rho_r + \overline{\gamma}_1] \end{cases} \tag{24}$$

where $\overline{\gamma}_1$ is an arbitrary positive constant and d_{fq} is defined in Equation (15).

The L_1 adaptive controller is constructed on the basis of Equations (19) and (21), with the L_1-norm condition satisfied.

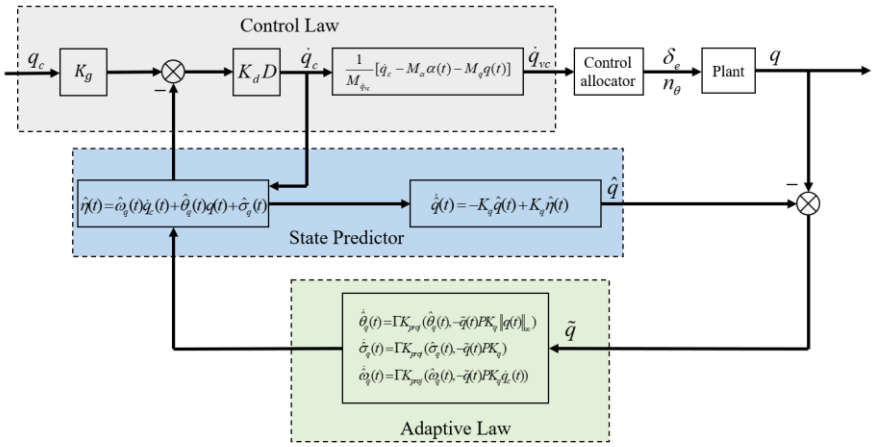

Figure 6. The L_1 adaptive controller architecture.

- Stability analysis

The stability analysis was performed using Lyapunov's second method, as described in Ref. [21].

Firstly, the tracking error the difference between the response of the state predictor (Equation (19)) and the control plant (Equation (14)), that is:

$$\begin{cases} \widetilde{q}(t) = \hat{q}(t) - q(t) \\ \dot{\widetilde{q}}(t) = -K_q\widetilde{q}(t) + K_q\widetilde{\eta}(t) \end{cases} \tag{25}$$

where $\widetilde{*}, * \in \{q, \dot{q}, \eta\}$ represents the tracking errors, $\widetilde{\eta}(t) = \hat{\eta}(t) - \eta(t)$. Given Equation (14), we have:

$$\widetilde{\eta}(t) = \hat{\eta}(t) - \eta(t) = \dot{q}_c(t)\widetilde{\omega}_q(t) + q(t)\widetilde{\theta}_q(t) + \widetilde{\sigma}_q(t) \tag{26}$$

with $\widetilde{\omega}_q(t) = \hat{\omega}_q(t) - \omega_q(t)$, $\widetilde{\theta}_q(t) = \hat{\theta}_q(t) - \theta_q(t)$ and $\widetilde{\sigma}_q(t) = \hat{\sigma}_q(t) - \sigma_q(t)$. The angular acceleration error is derived by substituting Equation (26) into Equation (25), that is:

$$\dot{\widetilde{q}}(t) = -K_q\widetilde{q}(t) + K_q[\dot{q}_c(t)\widetilde{\omega}_q(t) + q(t)\widetilde{\theta}_q(t) + \widetilde{\sigma}_q(t)] \tag{27}$$

The goal of adaptive laws is to drive the $\widetilde{\omega}(t)$, $\widetilde{\theta}(t)$ and $\widetilde{\sigma}(t)$ tend to zero to achieve stable error dynamics $\dot{\widetilde{q}}(t) = -K_q\widetilde{q}(t)$.

The candidate Lyapunov function is formulated as:

$$V(\widetilde{q}, \widetilde{\omega}_q, \widetilde{\theta}_q, \widetilde{\sigma}_q) = \widetilde{q}^T(t)P\widetilde{q}(t) + \frac{1}{\Gamma}(\widetilde{\omega}_q{}^2(t) + \widetilde{\theta}_q{}^2(t) + \widetilde{\sigma}_q{}^2(t)) \tag{28}$$

The time derivatives of Equation (28) is:

$$\dot{V}(\widetilde{q}, \widetilde{\omega}_q, \widetilde{\theta}_q, \widetilde{\sigma}_q) = \dot{\widetilde{q}}^T(t)P\widetilde{q}(t) + \widetilde{q}^T(t)P\dot{\widetilde{q}}(t) + \frac{2}{\Gamma}(\widetilde{\omega}_q(t)\dot{\widetilde{\omega}}_q(t) + \widetilde{\theta}_q(t)\dot{\widetilde{\theta}}_q(t) + \widetilde{\sigma}_q(t)\dot{\widetilde{\sigma}}_q(t)) \tag{29}$$

It is assumed that ω_q, θ_q and σ_q vary slowly enough to satisfy $\dot{\widetilde{\omega}}_q \approx \dot{\omega}_q$, $\dot{\widetilde{\theta}}_q \approx \dot{\hat{\theta}}_q$, $\dot{\widetilde{\sigma}}_q \approx \dot{\hat{\sigma}}_q$. Substituting Equation (27) into Equation (29), we get

$$\begin{aligned} \dot{V}(\widetilde{q}, \widetilde{\omega}_q, \widetilde{\theta}_q, \widetilde{\sigma}_q) = \; & \left\{-\widetilde{q}^T(t)K_q^T + [\widetilde{\omega}_q{}^T(t)\dot{q}_c{}^T(t) + \widetilde{\theta}_q{}^T(t)q^T(t) + \widetilde{\sigma}_q{}^T(t)]K_q^T\right\}P\widetilde{q}(t) \\ & + \widetilde{q}^T(t)P\left\{-K_q\widetilde{q}(t) + K_q[\dot{q}_c(t)\widetilde{\omega}_q(t) + q(t)\widetilde{\theta}_q(t) + \widetilde{\sigma}_q(t)]\right\} \\ & + \tfrac{2}{\Gamma}(\widetilde{\omega}_q{}^T(t)\dot{\hat{\omega}}_q(t) + \widetilde{\theta}_q{}^T(t)\dot{\hat{\theta}}_q(t) + \widetilde{\sigma}_q{}^T(t)\dot{\hat{\sigma}}_q(t)) \end{aligned} \tag{30}$$

With adaptive law defined in Equations (20) and (24), Equation (30) is re-constructed as

$$\begin{aligned}\dot{V}(\widetilde{q},\widetilde{\omega}_q,\widetilde{\theta}_q,\widetilde{\sigma}_q) = \quad & -\widetilde{q}^T(t)Q\widetilde{q}(t) + 2\widetilde{\omega}_q(t)(\widetilde{q}^T(t)PK_q\dot{q}_c{}^T(t) \\ & +K_{proj}(\hat{\omega}_q(t), -\widetilde{q}^T(t)PK_q\dot{q}_c(t))) \\ & +2\widetilde{\theta}_q{}^T(t)(q(t)\widetilde{q}^T(t)PK_q + K_{proj}(\hat{\theta}_q(t), -q(t) - \widetilde{q}^T(t)PK_q)) \\ & +2\widetilde{\sigma}_q{}^T(t)(\widetilde{q}^T(t)PK_q + K_{proj}(\hat{\sigma}_q(t), -\widetilde{q}^T(t)PK_q)) \\ & -\tfrac{2}{\Gamma}(\widetilde{\omega}_q{}^T(t)\dot{\omega}_q(t) + \widetilde{\theta}_q{}^T(t)\dot{\theta}_q(t) + \widetilde{\sigma}_q{}^T(t)\dot{\sigma}_q(t))\end{aligned} \tag{31}$$

The projection operator in the adaptive laws ensures that the adaptive parameters are limited to a known compact set Λ. The projection operator is written as $\dot{\theta}_q(t) = K_{proj}(\theta_q, \Gamma z)$, and the properties of the projection function guarantee that for any point $\theta_q(\tau_1) \in \Lambda$, where $\tau_1 \in [0, t)$ and z is a parameter. Then, we have:

$$(\theta_q - \theta_q(\tau_1))^T(\Gamma^{-1}K_{proj}(\theta_q, \Gamma z) - z) \leq 0 \tag{32}$$

With (32), Equation (31) can be simplified to an inequation:

$$\dot{V}(\widetilde{q},\widetilde{\omega}_q,\widetilde{\theta}_q,\widetilde{\sigma}_q) \leq -\widetilde{q}^T(t)Q\widetilde{q}(t) + \frac{2}{\Gamma}(\left|\widetilde{\omega}_q{}^T(t)\dot{\omega}_q(t) + \widetilde{\theta}_q{}^T(t)\dot{\theta}_q(t) + \widetilde{\sigma}_q{}^T(t)\dot{\sigma}_q(t)\right|) \tag{33}$$

As ω_q is a constant, $\dot{\omega}_q = 0$. Then, (33) can be expressed as:

$$\dot{V}(\widetilde{q},\widetilde{\omega}_q,\widetilde{\theta}_q,\widetilde{\sigma}_q) \leq -\widetilde{q}^T(t)Q\widetilde{q}(t) + \frac{2}{\Gamma}(\left|\widetilde{\theta}_q{}^T(t)\dot{\theta}_q(t) + \widetilde{\sigma}_q{}^T(t)\dot{\sigma}_q(t)\right|) \tag{34}$$

According to the bounds Equations (17) and (18) defined in Lemma 1, function (34) is simplified as:

$$\dot{V}(\widetilde{q},\widetilde{\omega}_q,\widetilde{\theta}_q,\widetilde{\sigma}_q) \leq -\widetilde{q}^T(t)Q\widetilde{q}(t) + \frac{4}{\Gamma}(d_{\mathrm{fq}}(\rho)d_\theta + bd_\sigma) \tag{35}$$

Using the properties of projection operator again, Equation (28) is reduced to an inequation as:

$$\widetilde{\omega}_q{}^2(t) + \widetilde{\theta}_q{}^2(t) + \widetilde{\sigma}_q{}^2(t) \leq (\omega_{qu} - \omega_{ql})^2 + 4d_{\mathrm{fq}}{}^2(\rho) + 4b^2 \tag{36}$$

The condition $\widetilde{q}(0) = 0$ derives

$$V(0) \leq \frac{1}{\Gamma}((\omega_{qu} - \omega_{ql})^2 + 4d_{\mathrm{fq}}(\rho)d_\theta + 4bd_\sigma) \tag{37}$$

Assume that:

$$V(t) > \frac{\lambda_m(\rho_r)}{\Gamma} \tag{38}$$

where $\lambda_m(\rho_r) \triangleq (\omega_{qu} - \omega_{ql})^2 + 4d_{\mathrm{fq}}{}^2(\rho) + 4b^2 + 4\frac{\lambda_{\max}(P)}{\lambda_{\min}(Q)}(d_{\mathrm{fq}}(\rho)d_\theta + bd_\sigma)$, $\lambda_{\max}(P)$ is the max eigenvalue of matrix P, and $\lambda_{\min}(P)$ is the min eigenvalue of matrix Q.

Substitute (36) and (38) into Equation (28) and you get:

$$\widetilde{q}^T(t)Q\widetilde{q}(t) \geq \frac{\lambda_{\max}(Q)}{\lambda_{\min}(P)}\widetilde{q}^T(t)P\widetilde{q}(t) \geq \frac{4}{\Gamma}(d_{\mathrm{fq}}(\rho)d_\theta + bd_\sigma) \tag{39}$$

Using (39) and (35) yields $\dot{V}(\widetilde{q},\widetilde{\omega}_q,\widetilde{\theta}_q,\widetilde{\sigma}_q) < 0$

Therefore, we have:

$$V(t) \leq V(0) \leq \frac{1}{\Gamma}((\omega_{qu} - \omega_{ql})^2 + 4d_{\mathrm{fq}}(\rho)d_\theta + 4bd_\sigma) \leq \frac{\lambda_m(\rho_r)}{\Gamma} \tag{40}$$

Since the result of Equation (40) contradicts the assumption of Equation (32), the actual assumption of Equation (38) should be rewritten as:

$$V(t) \leq \frac{\lambda_m(\rho_r)}{\Gamma} \tag{41}$$

The Lyapunov second method indicates that the system satisfying (41) is stable.

3.2. Control Allocation

A control allocator is designed to determine the command of the actuators based on the angular rate command generated by the CSAS. For the abundant control actuators in all channels, the allocation criterion uses the efficiency of the actuators, which is related to the airspeed, to determine the actuator commands.

Since the body frame of the ET120 is almost symmetrical, the products of inertia J_{xy}, J_{yz} and J_{zx} can be ignored, and the virtual commands to the actuators in the roll, pitch and yaw channels can be given according to the outputs of the controllers in corresponding channels $\dot{p}_c$, $\dot{q}_c$ and $\dot{r}_c$:

$$\begin{cases} \delta_a = \frac{\dot{p}_c}{L_{\max}} \delta_a^{\min} \\ \delta_e = \frac{\dot{q}_c}{M_{\max}} \delta_e^{\min} \\ \delta_r = \frac{\dot{r}_c}{N_{\max}} \delta_r^{\max} \end{cases}, \begin{cases} n_\phi = \frac{\dot{p}_c}{L_{\max}} n_\phi^{\max} \\ n_\theta = \frac{\dot{q}_c}{M_{\max}} n_\theta^{\max} \\ n_\varphi = \frac{\dot{r}_c}{N_{\max}} n_\phi^{\max} \end{cases} \tag{42}$$

where the superscript max and min represent the maximum or minimum outputs of the corresponding controllable variables.$L_{\max}$, $M_{\max}$ and $N_{\max}$ represent the maximum control effectiveness in the roll, pitch, and yaw channels, respectively, and are given by the following equations:

$$\begin{cases} L_{\max} = \eta_{\delta_a} \overline{L}_{\delta_a} \delta_a^{\min} + \overline{L}_{n_\phi} n_\phi^{\max} \\ M_{\max} = \eta_{\delta_e} \overline{M}_{\delta_e} \delta_e^{\min} + \overline{M}_{n_\theta} n_\theta^{\max} \\ N_{\max} = \overline{N}_{\delta_r} \delta_r^{\max} + \overline{N}_{n_\varphi} n_\varphi^{\max} \end{cases} \tag{43}$$

where $\overline{L}_{\delta_a}$, $\overline{M}_{\delta_e}$, $\overline{N}_{\delta_r}$, are the moments provided by each unit deflection of the corresponding control surface in roll, pitch, and yaw channels. $\overline{L}_{n_\phi}$, $\overline{M}_{n_\theta}$, $\overline{N}_{n_\varphi}$ are the moments produced by each unit's virtual control inputs for the rotors in the roll, pitch, and yaw channels. η_{δ_a} and η_{δ_e} are gain-scheduled coefficients that are relevant to the airspeed V_t.

4. Deceleration Transition Process Maneuver Design

4.1. Process Analysis and Maneuver Design

The currently used deceleration and landing process for the ET120 vehicle is depicted in Figure 7. The process begins from level flight in fixed-wing cruising mode. When the autonomous landing logic of the autopilot is activated, the ET120 vehicle turns off the propulsion rotor and performs the pitch-up maneuver. In the early stage of deceleration, a large pitch-up input increases the angle of attack at the cruising speed (usually at a high airspeed), which produces a large aerodynamic lift (more than the aircraft weight), resulting in climbing behavior. This is done for two reasons. One is to transform the kinetic energy into potential energy by increasing altitude. Another is to cut off the forward thrust force to reduce the kinetic energy input, so the decrease in airspeed is accompanied by an increase in altitude. When the airspeed is reduced to near the hover decision speed, the ET120 vehicle follows the multi-rotor hover mode in preparation for vertical descent and final landing. This strategy has the following shortcomings: 1. The deceleration corridor is a straight and long line, which imposes restrictions on high-density traffic in terminal airspace. 2. The increase in altitude goes against the common sense of decreasing altitude during the landing process. 3. The increase in altitude also consumes more battery energy and increases the workload of the hovering rotors, resulting in lower flight performance.

4. It is also a very poor driving experience for passengers. This ragged deceleration strategy is obviously not suitable for urban transportation.

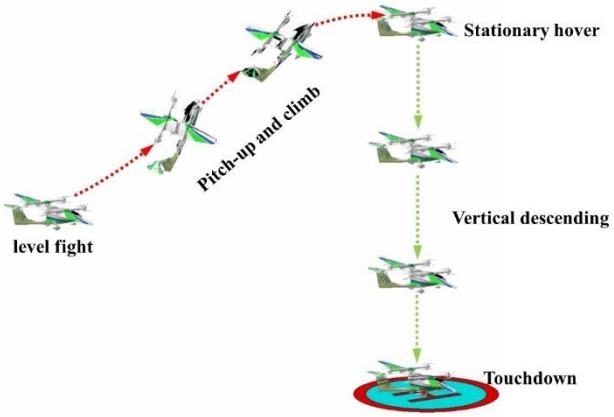

Figure 7. Conventional jumping deceleration and landing process.

A major improvement would be to avoid the climbing behavior caused by the large lift. One idea is to perform a fast pull-up maneuver like a fighter jet to cause the ET120 vehicle to enter post-stall flight, as shown in Figure 8. Instead of the pitch-up motion, the large normal overload input quickly produces a large AOA, and thus a large drag that leads to a continuous drop in lift and airspeed. When the AOA exceeds the stall AOA, the ET120 vehicle falls into a stall flight maneuver and re-engages to hover stationary in preparation for vertical descent to the landing pad (vertiport). During this deceleration process, the altitude can be slightly perturbed. However, this extreme deceleration approach comes at the expense of safety and reliability, and is not suitable for urban transportation.

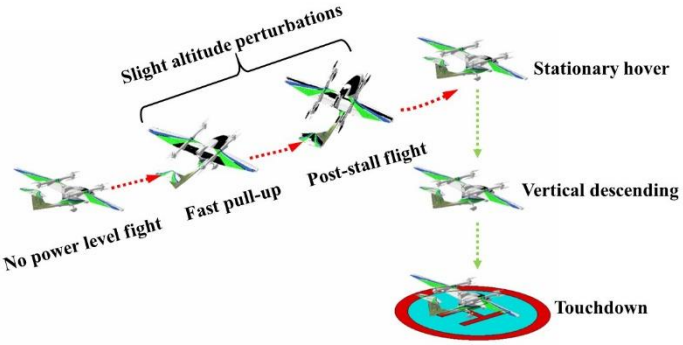

Figure 8. High AOA post-stall maneuver deceleration and landing process.

Another idea is to bank the ET120 vehicle to cleverly guide the large lift caused by pitch-up motion sideways, just like the bank-to-turn technology for missile autopilot. This allows the ET120 vehicle to turn the maximum lift plane and project the partial lift (used to balance the gravity) to the longitudinal (vertical) plane to suppress climbing tendency.

Motivated by the above analysis, a five-stage spiral control strategy for a comfortable deceleration transition and landing process is designed for the ET120 vehicle, as shown in Figure 9. The logic begins from a fixed-wing cruise flight at Point A, after thoroughly performing five stages, the ET120 vehicle finally vertically touches down on the landing pad, at Point F. The main five-stage spiral control strategy is as follows:

- Stage I: (red dotted lines)

Stage I is used to get close to the landing pad from far away. At Point A, the ET120 vehicle begins to bank and enter a turn to track the loiter circle centered on the landing pad in fixed-wing flight mode. The turn ends at Point B, when the cross-track error from

the current position to the loiter circle is less than 3 m. At this stage, altitude and airspeed maintain constant.

- Stage II: (green dotted lines)

In stage II, the aircraft begins to enter the deceleration transition phase. At point B, the ET120 vehicle turns off the propulsion rotor and enters no-power flight in fixed-wing mode. It also maintains a fixed altitude to increase the AOA and thus increase the drag to reduce airspeed. Meanwhile, a fixed bank angle ϕ_0 is set to spirally turn toward the landing pad. This stage ends at Point C, where the pitch angle reaches the set value θ_0.

- Stage III: (blue dotted lines)

During this stage, the ET120 vehicle is still in mid-airspeed flight, and the efficiency of aero-surface is far greater than the multi-rotors. The multi-rotors are activated, and their throttle is set to 30% of the maximum throttle. Meanwhile, the bank angle is fixed at ϕ_1 to continue turning, and it continues to maintain altitude to reduce airspeed. This stage ends at Point D, when the pitch angle reaches the set value θ_1.

- Stage IV: (yellow dotted lines)

At this stage, the ET120 vehicle is in mid- to low-airspeed flight, and the efficiency of the aero-surface is equal to the multi-rotors. Then, the throttle of the multi-rotors is set to 60% of the maximum throttle. It enters rotor mode, and the altitude is controlled by the multi-rotors. Meanwhile, the aircraft begins to align its nose to the route via attitude motion. This stage ends at Point E, when the airspeed is less than 5 m/s.

- Stage V: (purple dotted lines)

At this stage, the ET120 vehicle engages a stationary hover state in preparation for vertical descent and touchdown. Once the vehicle receives the landing instruction, it commences vertical descent to the landing pad at Point F.

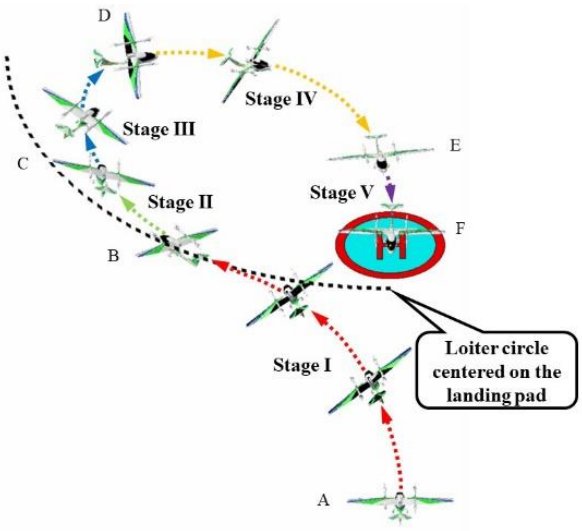

Figure 9. Five stages of the roll-horizon deceleration and landing strategy.

4.2. Control Module Design

- Stage I:

In stage I, it is necessary to design the lateral guidance law to guide the ET120 to the loiter circle in fixed-wing flight mode, as shown in Figure 10. The typical implementation of lateral guidance converts the cross-track error and the track angle error to the acceleration reference. The controller for lateral channel is designed via a cascaded-loop form. The cross-track error, Δy, and the desired track angle reference, ψ_d, are inputs of the lateral channel, and the desired lateral acceleration command, $a_{y,c}$, is the output command.

The desired lateral speed, $\dot{y}_d$, is first obtained from the cross-track error Δy:

$$\dot{y}_d = k_{Py}\Delta y \tag{44}$$

where k_{Py} is the proportional gain, and Equation (44) expects the cross-track error to converge linearly according to the time constant $1/k_{py}$.

Then, the desired track angle caused by lateral motion, $\Delta\psi_c$, can be converted as:

$$\Delta\psi_c = \sin^{-1}(\dot{y}_d/V_g) \tag{45}$$

where V_g is groundspeed. $\Delta\psi_c$ is usually considered to be small, and can be approximated as $\Delta\psi_c = \dot{y}_d/V_g$, which is also limited to $[-\pi/2, \pi/2]$. ψ_c is combined with the desired track angle reference, ψ_d, to form a track angle command ψ_c.

$$\psi_c = \psi_d + \Delta\psi_c \approx \psi_d + \dot{y}_d/V_g \tag{46}$$

Then, the lateral acceleration command a_{yc} can be constructed as:

$$a_{yc} = k_{P\psi}(\psi_c - \psi)V_g \tag{47}$$

where $k_{P\psi}$ is proportional gain and $(\psi_c - \psi)$ should be limited to $[-\pi, \pi]$.

With a coordinated turn assumption, the lateral acceleration command a_{yc} can be converted to a roll angle command ϕ_c.

$$\phi_c = \tan^{-1}(a_{yc}/g) \tag{48}$$

where g is acceleration of gravity.

In the roll angle controller, ϕ is controlled by a proportional control:

$$\dot{\phi}_c = k_{P\phi}(\phi_c - \phi) \tag{49}$$

where $k_{P\phi}$ is proportional gain.

Then, the relationship of Euler angular rates to body angular rates are constructed as:

$$\begin{cases} \dot{\phi} = p + \tan\theta(q\sin\phi + r\cos\phi) \\ \dot{\theta} = q\cos\phi - r\sin\phi \\ \dot{\psi} = (q\sin\phi + r\cos\phi)/\cos\theta \end{cases} \tag{50}$$

From Equation (50), the desired roll angular rate p_c can be calculated as

$$p_c = \dot{\phi}_c - \tan\theta(q\sin\phi + r\cos\phi) \tag{51}$$

For the yaw channel, a yaw damper is designed to improve the damping features of the Dutch roll. In addition, a high-pass filter is also added to weaken the steady yaw angular rate signal by the stable loiter. The controller is constructed as:

$$\delta_r = k_{Pr}\frac{\tau s}{\tau s + 1} \tag{52}$$

where k_{Pr} is proportional gain, and τ is time constant of high pass filter.

In the altitude channel, the fixed-wing implementations of the altitude motion are achieved via the path angle change. The inputs for the altitude control channel are the altitude h, the climbing rate $\dot{h}$, and the desired path climbing rate reference $\dot{h}_d$. The output is the path angle command γ_c.

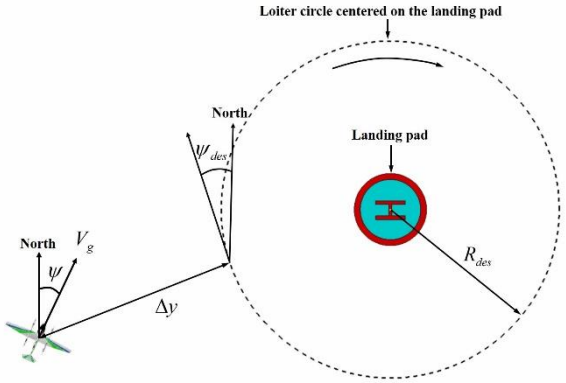

Figure 10. The lateral guidance principle in fixed-wing mode.

As in the design of the lateral channel, the desired climbing rate command is constructed as:

$$\dot{h}_c = k_{Ph}(h_d - h) + \dot{h}_d \tag{53}$$

where k_{Ph} is proportional gain. It is the converted to path angle command γ_c:

$$\gamma_c = \tan^{-1}\theta\left(\dot{h}_c / V_g\right) \tag{54}$$

Then, pitch angle control is achieved via a proportional-integral controller, organized as:

$$\theta_c = k_{P\gamma}(\gamma_c - \gamma) + k_{I\gamma}\int {}_0^t(\gamma_c - \gamma)d\tau \tag{55}$$

where $k_{P\gamma}$ is proportional gain; $k_{I\gamma}$ is integral gain.

Similarly to the roll channel, θ is also controlled via a proportional controller:

$$\dot{\theta}_c = k_{P\theta}(\theta_c - \theta) \tag{56}$$

where $k_{P\theta}$ is proportional gain; $\dot{\theta}_c$ is pitch angular rate command.

From Equation (50), the desired pitch angular rate q_c can be calculated as:

$$q_c = \frac{\dot{\theta}_c}{\cos\phi} + r\tan\phi \tag{57}$$

For the airspeed channel, the desired airspeed reference V_{td} is controlled via a proportional-integral controller. The input is airspeed V_t and the output is throttle command δ_t.

$$\delta_t = k_{Pv}(V_{td} - V_t) + k_{Iv}\int (V_{td} - V_t)dt \tag{58}$$

where k_{Pv} is proportional gain and k_{Iv} is integral gain.

In addition, the hover rotor speed command n_h is set to zero. The above commands together form $\boldsymbol{U} = [p_c, q_c, \delta_r, \delta_t, n_h = 0]$ for the reference input of the angular rate loop.

- Stage II:

In stage II, the ET120 enters fixed-wing gliding flight mode. The ET120 turns off the propulsion rotor and maintains a fixed bank angle, ϕ_0, at the end of Stage I. In general, the altitude channel is similar as that in Stage I. In addition, the hovering and propulsion rotors are set zero. By combining Equations (51), (52) and (57), p_c, q_c and δ_r are derived in the output $\boldsymbol{U}$. Then, the new $\boldsymbol{U}$ is organized as $\boldsymbol{U} = [p_c, q_c, \delta_r, \delta_t = 0, n_h = 0]$ for the reference input of the angular rate loop.

- Stage III:

In Stage III, the ET120 reaches the set pitch angle θ_0 at the end of Stage II. Correspondingly, the airspeed is reduced to mid speed. At this stage, the control module is similar to that in Stage II; in addition, an open-loop hovering rotor system is applied.

The hovering rotor command is set to $\delta_t = 30\%$ and the roll angle is fixed at $\phi = \phi_0$. By combining Equations (51), (52) and (57), p_c, q_c and δ_r are derived in the output $\boldsymbol{U}$. Then, the new $\boldsymbol{U}$ is organized as $U = [p_c, q_c, \delta_r, \delta_t = 0, n_h = 30\%]$ for the reference input of the angular rate loop.

- Stage IV:

In Stage IV, the ET120 reaches the set pitch angle θ_1 at the end of Stage III. In addition, it is in mid- to low-airspeed flight. The hovering rotor system gradually occupies the dominant position of the control capability. The autopilot puts ET120 into rotor mode.

The control of forward speed is achieved by body pitch, and control of altitude is performed via total hovering rotor thrust. In addition, the roll angle is fixed at $\phi = \phi_1$. For the design of altitude channel, the desired climbing rate command, $\dot{h}_c$, is first obtained from Equation (53). It is then used to derive the vertical acceleration command a_{hc} via a proportional controller.

$$a_{hc} = k_{Pa_h}\left(\dot{h}_c - \dot{h}\right) \tag{59}$$

where k_{Pa_h} is a proportional gain.

The inputs for forward speed channel are groundspeed V_g and its command V_{gc}, and the output is θ_c via a Proportional-Integral controller. The forward acceleration is first calculated from forward speed error:

$$a_{xc} = k_{PV_g}(V_{gc} - V_g) + k_{IV_g}\int_0^t (V_{gc} - V_g)d\tau \tag{60}$$

where k_{PV_g} is a proportional gain, and k_{IV_g} is an integral gain.

The a_{xc} is usually small and the approximate relationship between a_{xc} and θ_c can be calculated as:

$$\theta_c \approx -\frac{a_{xc}}{g} \tag{61}$$

The control of θ_c is mentioned in Stage 1.

In addition, the roll angle is fixed at $\phi = \phi_1$. To control yaw channel, a proportional controller is applied. The heading angle can be derived as:

$$\dot{\psi}_c = k_{P\varphi}\left(\tan^{-1}(V_e/V_n) - \varphi\right) \tag{62}$$

where $k_{P\varphi}$ is a proportional controller.

From Equation (50), the yaw rate command can be calculated as:

$$r_c = \frac{\dot{\psi}_c \cos\theta - q\sin\phi}{\cos\phi} \tag{63}$$

where r_c is then inserted into $\boldsymbol{U} = [p_c, q_c, r_c, \delta_t, n_h]$ for output to the reference input of the angular rate loop.

The hovering rotors are set 60%. By combining Equations (51) and (57), p_c and q_c are derived in the output $\boldsymbol{U}$. Then, the new $\boldsymbol{U}$ is organized as $\boldsymbol{U} = [p_c, q_c, r_r, \delta_t = 0, n_h]$ for the reference input of the angular rate loop.

- Stage V:

In stage V, the ET120 enters stationary hover mode. The lateral position in this stage should be controlled to within the landing window. Implementation of the guidance algorithm is depicted in Figure 11. Control of forward position is driven by body pitch,

and control of lateral position is achieved via body roll. In addition, its heading aligns with the reference route via body yaw.

In the control module, the desired lateral speed, $\dot{y}_d$, and forward speed, $\dot{x}_d$ are first acquired from cross-track error, Δy and forward distance error Δx:

$$\begin{cases} \dot{y}_d = k_{Py}\Delta y \\ \dot{x}_d = k_{Px}\Delta x \end{cases} \tag{64}$$

where k_{Px} is proportional gain.

Then, we project the $\dot{y}_d$, $\dot{x}_d$ and ground speed into the ET120's direction of movement to acquire forward speed error, $\Delta\dot{x}$ and lateral speed error, $\Delta\dot{y}$:

$$\begin{cases} \Delta\dot{x} = \dot{x}_d\cos(\psi-\psi_d) + \dot{y}_d\sin(\psi-\psi_d) - V_n\cos(\psi) - V_e\sin(\psi) \\ \Delta\dot{y} = (\dot{y}_d)\sin(\psi-\psi_d) + (\dot{y}_d)\cos(\psi-\psi_d) - V_e\cos(\psi) + V_n\sin(\psi) \end{cases} \tag{65}$$

These are then used to derive forward and lateral acceleration commands, a_{xc} and a_{yc}, respectively:

$$\begin{cases} a_{xc} = k_{P\dot{x}}(\Delta\dot{x}) + k_{I\dot{x}}\int_0^t(\Delta\dot{x})d\tau \\ a_{yc} = k_{P\dot{y}}(\Delta\dot{y}) + k_{I\dot{y}}\int_0^t(\Delta\dot{y})d\tau \end{cases} \tag{66}$$

where $k_{P\dot{x}}$ and $k_{P\dot{y}}$ are proportional gains. $k_{I\dot{x}}$ and $k_{I\dot{y}}$ are integral gains.

The a_{xc} and a_{yc} are usually limited to be numerically small, and the approximate relationship between $a_{xc}(a_{yc})$ and $\theta_c(\phi_c)$ can be calculated as:

$$\begin{cases} \theta_c \approx -\frac{a_{xc}}{g} \\ \phi_c \approx \frac{a_{yc}}{g} \end{cases} \tag{67}$$

The control of θ_c and ϕ_c are mentioned in Stage 1.

To control yaw channel, a proportional controller is applied. The heading angle can be derived as:

$$\dot{\psi}_c = k_{P\psi}(\psi_c - \psi) \tag{68}$$

From Equation (50), the yaw rate command can be calculated as:

$$r_c = \frac{\dot{\psi}_c\cos\theta - q\sin\phi}{\cos\phi} \tag{69}$$

r_c is then inserted into $\boldsymbol{U} = [p_c, q_c, r_c, \delta_t, n_h]$ for output to the reference input of the baseline L_1 adaptive controllers.

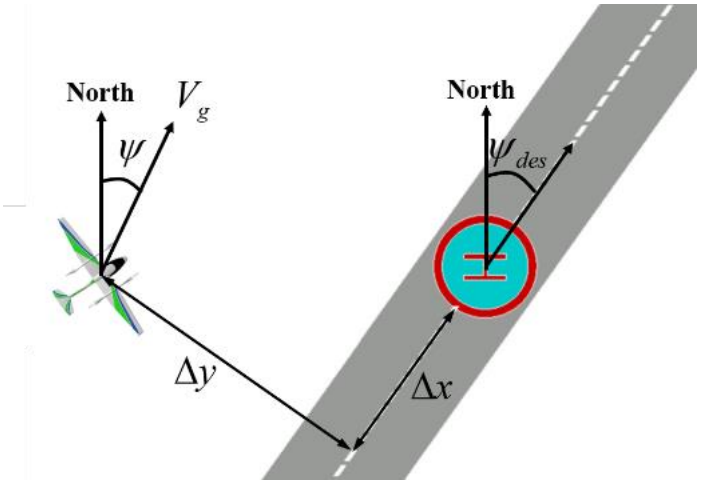

Figure 11. The lateral guidance principle in multi-rotor mode.

The control logic of the roll-horizon deceleration process is illustrated in Figure 12, mainly describing the guidance, control mode and path plans.

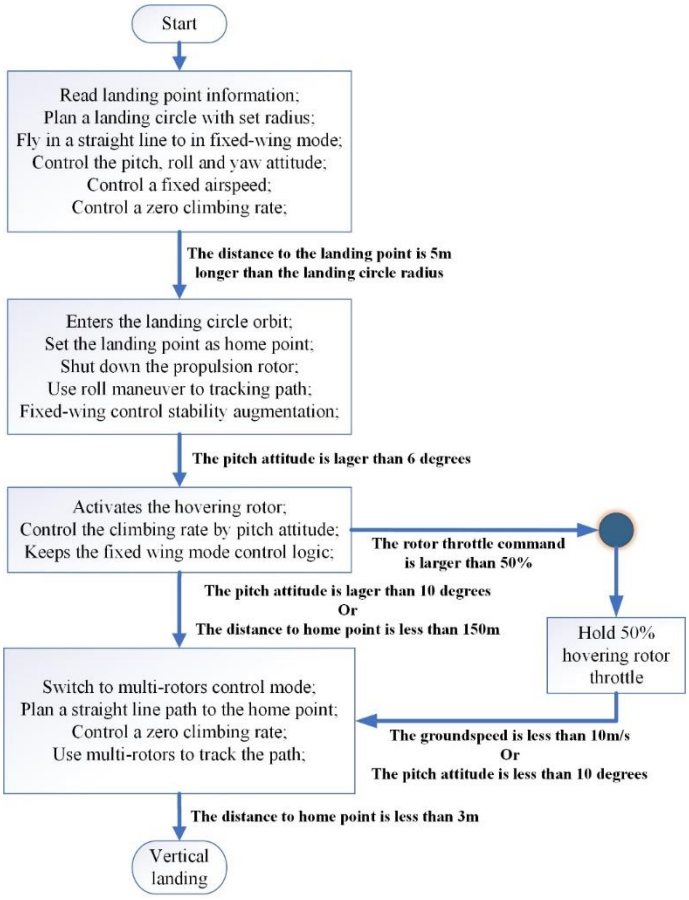

Figure 12. The roll-horizon deceleration logic.

The complete control scheme for deceleration transition and landing process is illustratively depicted in Figure 13. It includes the L_1 angular rate adaptive controller and the corresponding control modules designed for the five stages of the deceleration landing process, which will be discussed in detail in the following sections. In Figure 13, each control module is marked with content-related sections and equations of the control algorithm.

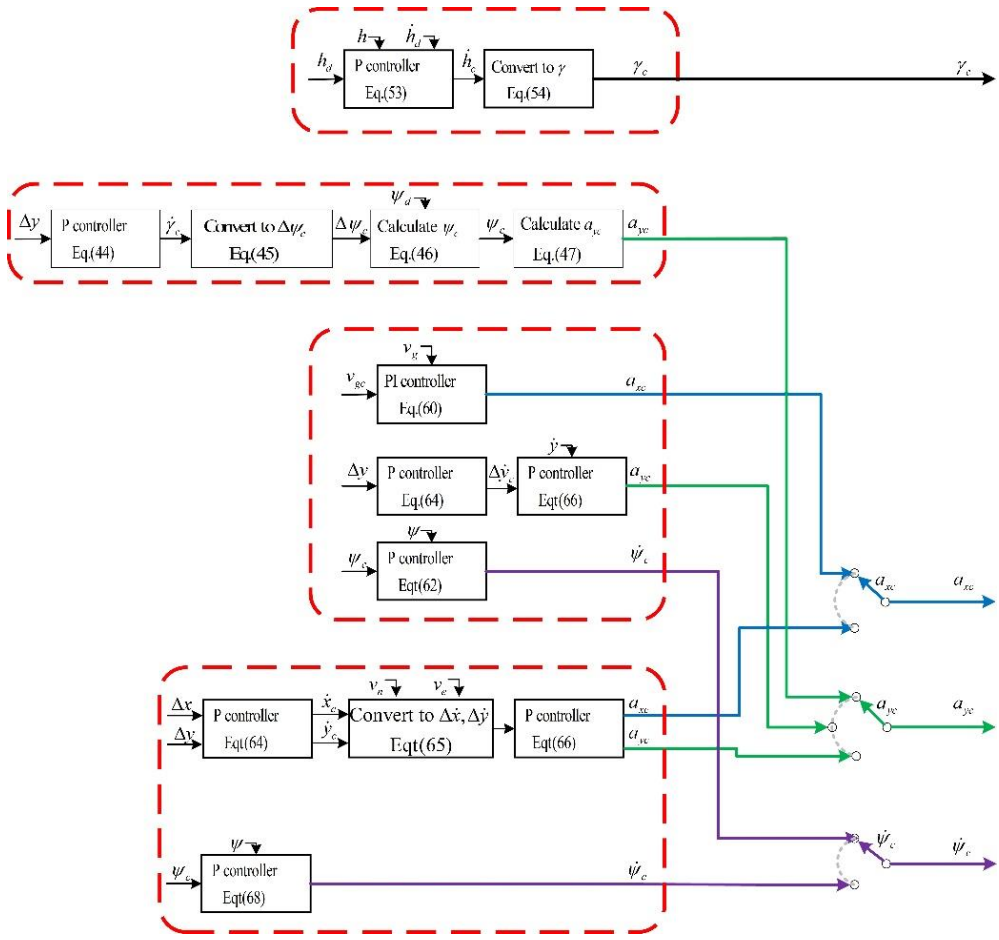

(**a**)

Figure 13. *Cont.*

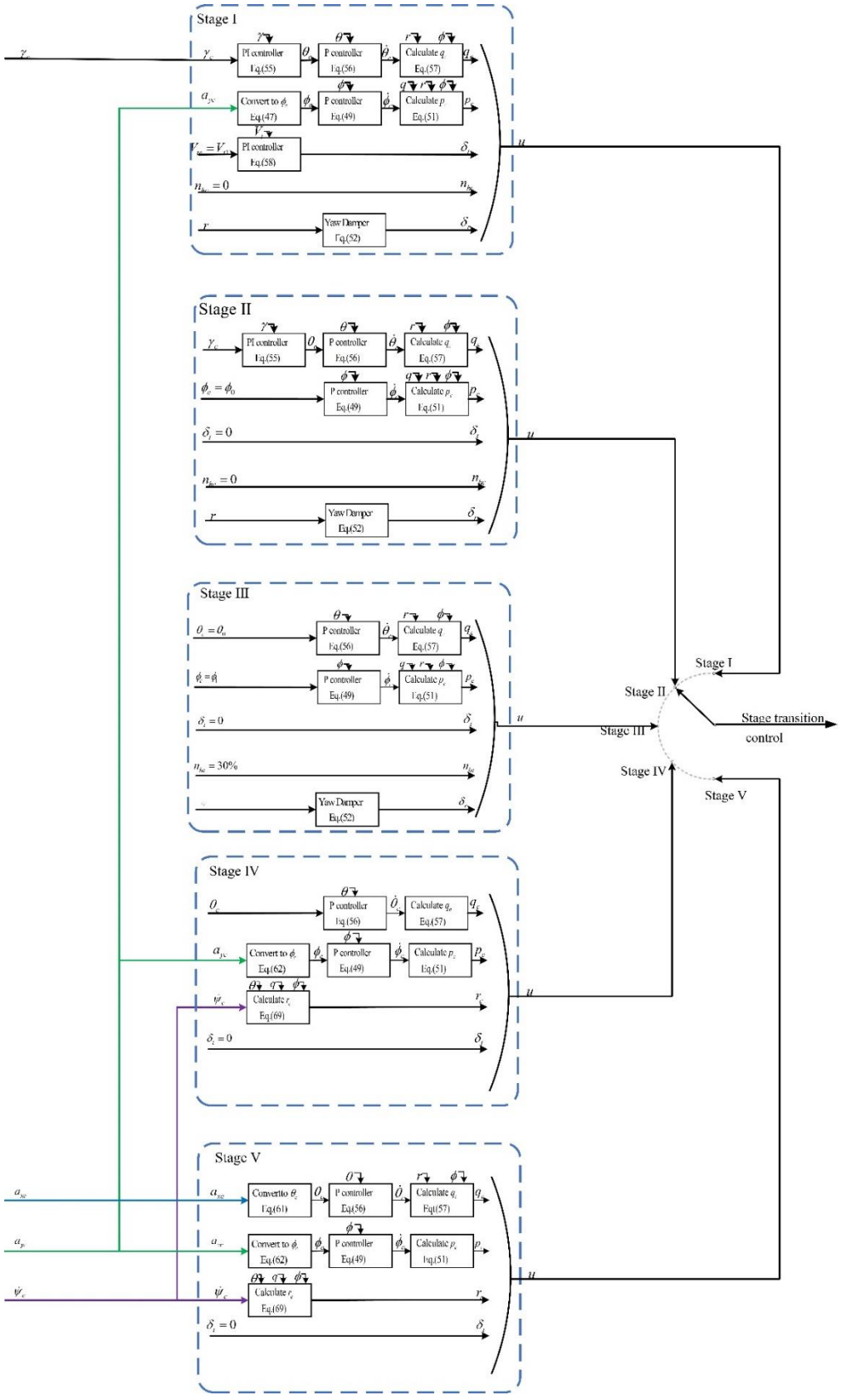

Figure 13. The control logic of the five-stage maneuver. (**a**) Guidance layer; (**b**) Strategy maneuver logic.

5. Simulation and Verification

5.1. Monte Carlo Simulations of Angular Rate L_1 Controller

The virtual control coefficient and virtual state coefficient contain the estimation of the model coefficients, influencing the tracking performance of the controller. Usually, the values of these factors are set empirically, which requires verification. This section takes the roll channel as an example to verify the parameter settings. The parameters to verify are the roll rate virtual control coefficient ω_p and virtual state coefficient K_p.

A 2 rad/s frequent square roll rate command was given as the input to an L_1 controller with $\Gamma = 2500$ and $D = 1/s$. The results for different combinations of ω_p and K_p are given in Figures 14 and 15. The numerical performance results are given in Table 4.

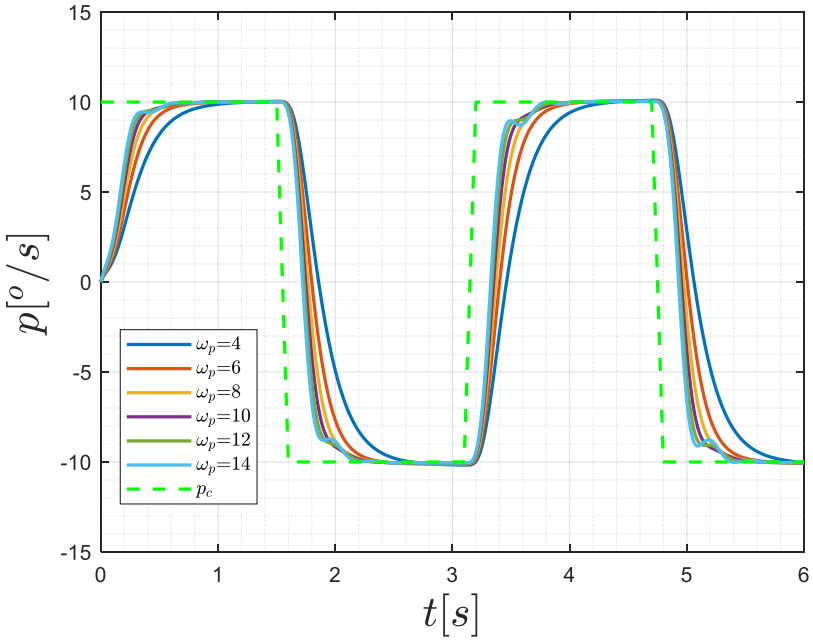

Figure 14. Time histories of roll rate with K_p = 8.

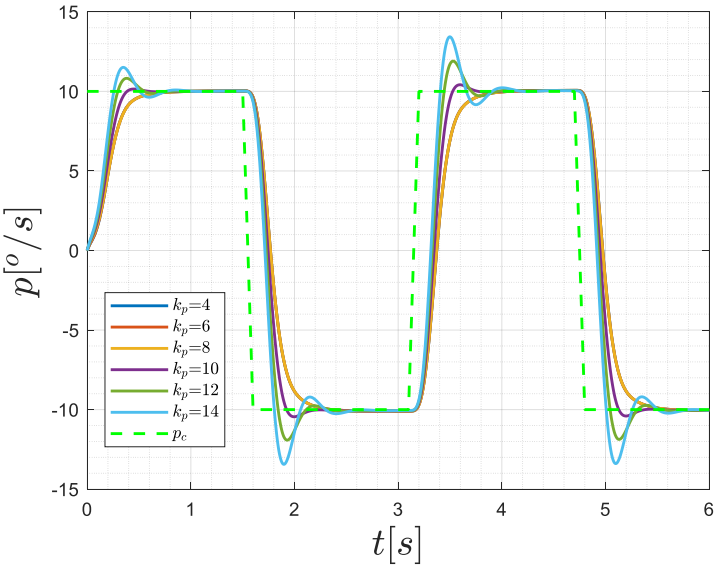

Figure 15. Time histories of roll rate with ω_p = 8.

Table 4. The performance of different L_1 parameters.

$[K_p,\omega_p]$	Risetime	Overshoot
[4,8]	1.17	-
[6,8]	0.72	-
[8,8]	0.65	-
[10,8]	0.63	-
[12,8]	0.62	-
[14,8]	0.6	-
[8,4]	1.14	-
[8,6]	0.78	-
[8,10]	0.63	1.5%
[8,12]	0.76	8%
[8,14]	0.85	15%

We chose $K_p = 8$, $\omega_p = 8$ as the values for the virtual control coefficient and virtual state coefficient, as these values make a tradeoff between rapidity and stability, with a small risetime and zero overshoots.

5.2. Monte Carlo Simulations of Angular Rate L_1 Controller

To verify the performance of the L_1 controller, a Monte Carlo simulation was executed. The modeling parameters that influence the control efficiency and trimming states were subjected to perturbation, because these factors are the most sensitive to the performance of control systems. The perturbation parameters are given in Table 5.

Table 5. The perturbation parameters.

Parameters	Perturbations
$C_{m_{\delta_e}}$	±20%
C_{m_α}	±20%
$C_{L_{\delta_e}}$	±20%
C_{S_β}	±20%
$C_{S_{\delta_r}}$	±20%
C_{l_β}	±20%
$C_{l_{\delta_a}}$	±20%
C_{l_p}	±50%
C_{l_r}	±50%
C_{n_β}	±20%
$C_{n_{\delta_r}}$	±20%
C_{n_p}	±50%
C_{n_r}	±50%
CG_x	±0.3 m
J_{xx}	±20%
J_{yy}	±20%
J_{zz}	±20%

1. percentages mean multiplication gain; 2. decimals mean addition value.

In Table 5, $C_{L_{\delta_e}}$, $C_{m_{\delta_e}}$, $C_{S_{\delta_r}}$, $C_{n_{\delta_r}}$, $C_{l_{\delta_a}}$ are the control derivatives, C_{m_α}, C_{S_β}, C_{l_β}, C_{n_β} are the stability derivatives, C_{l_p}, C_{n_r} are the damping derivatives, C_{l_r}, C_{n_p} are the cross damping derivatives, CG_x is the center of gravity position in body x-axis, and J_{xx}, J_{yy}, J_{zz} are the inertia moments.

The simulation states of the three flight modes are given as:

- Fixed-wing: airspeed 35 m/s.
- Transition: airspeed 10 m/s.
- Multi-rotor: airspeed 0 m/s.

The tracking performances are tested with continuous reversed step commands:

- Roll angle command: 0° at 0 s, 25° at 5 s, −25° at 12 s, 0° at 20 s.

- Pitch angle command: 0° at 0 s, 10° at 5 s, -10° at 12 s, 0° at 20 s.

The simulation results of the three flight modes are depicted in Figures 16–18.

The results show that (1) the distribution of the attitude angles is narrow, which indicates a strong robustness of the L_1 controller, which is able to reject the perturbation listed above; (2) the tracking performance of the L_1 controller is excellent, with a steady state error of zero and a trivial time latency.

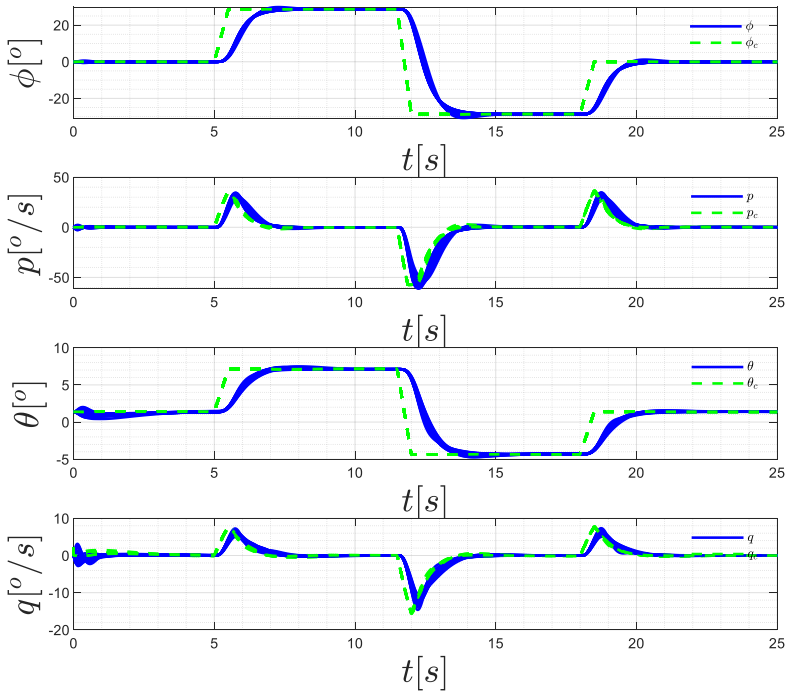

Figure 16. Time histories of longitudinal and lateral flight parameters in fixed–wing mode.

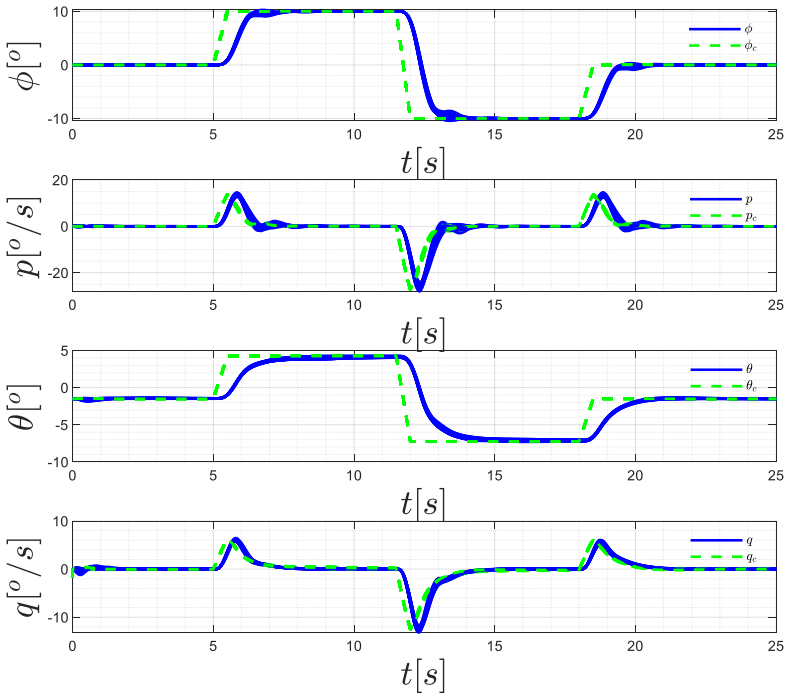

Figure 17. Time histories of longitudinal and lateral flight parameters in transitional mode.

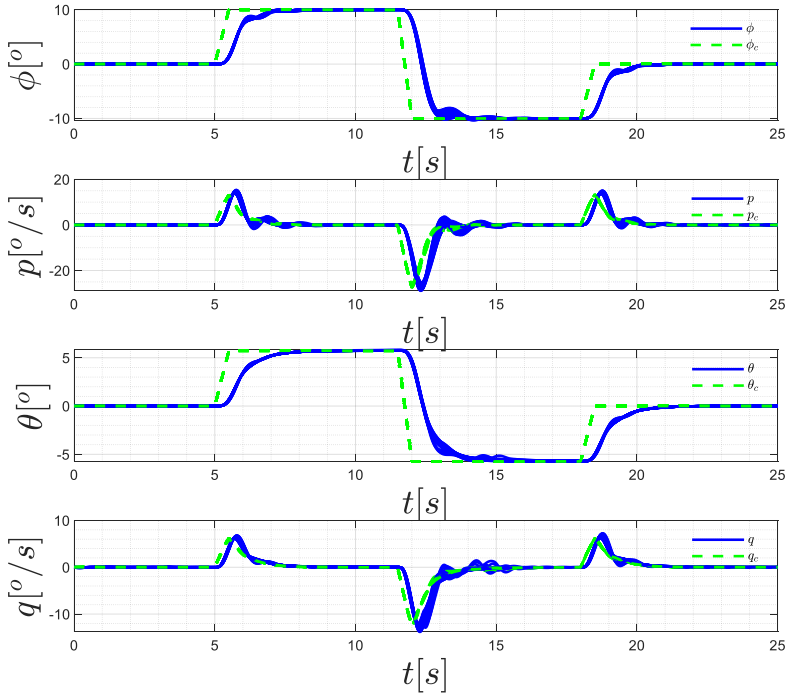

Figure 18. Time histories of longitudinal and lateral flight parameters in multi–rotor mode.

5.3. Simulations for Flight Path Verification

In practical applications, an eVTOL may enter vertiports in different initial states, namely with respect to cruise speed and landing circle radius. A feasible deceleration strategy should constrain the endings of the deceleration phase in the landing window for vertical landing in any possible initial states. To verify this, possible ranges of cruise speed and landing circle radius were set for the simulation as:

- Cruise airspeed: 30 m/s~50 m/s.
- Landing circle radius: 240 m~300 m.

The horizontal flight path results are given in Figure 19. It can be seen that the endings of all curves are distributed in a limited area, located in the landing window. These excellent results ensure a precise landing for vertiport management.

5.4. Monte Carlo Simulations of Rolling-Horizon Deceleration and Landing Strategy

Monte Carlo simulations are a common practice for robustness performance verification. The stability derivatives, control derivatives and damping derivatives are sensitive to the baseline angular rate control, but count for little in trajectory planning, while the basic values of the aerodynamic forces influence the deceleration efficiency and climbing rate control, which are sensitive to the trajectory results of the strategy; only the basic values of the aerodynamic forces C_{L_0}, C_{D_0}, C_{S_0} are perturbed in this simulation. The perturbation parameters are given in Table 6.

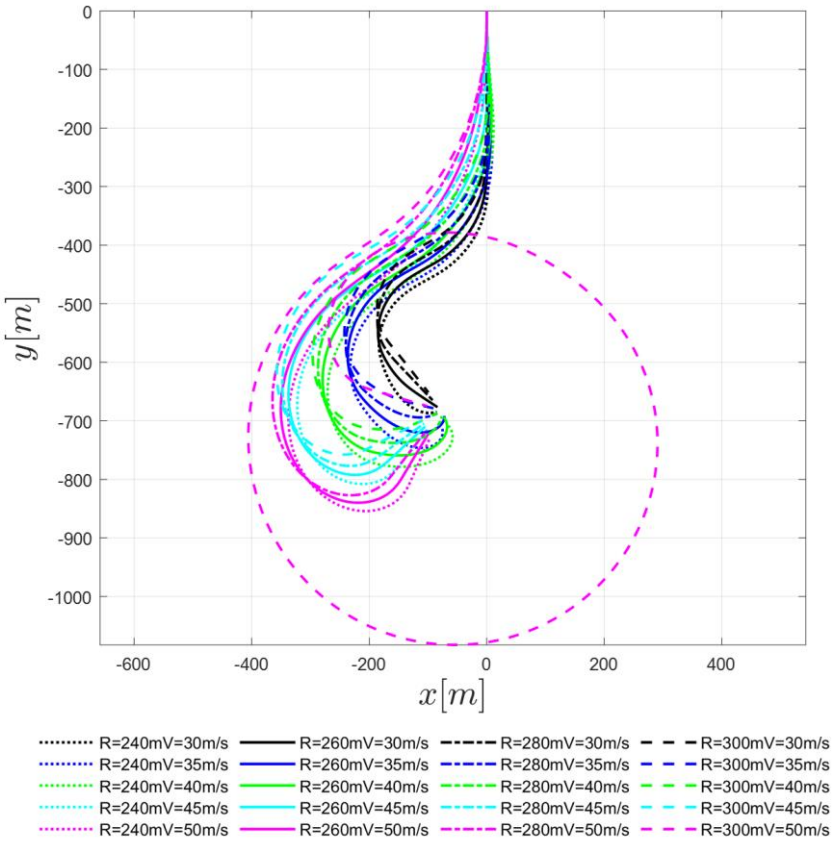

Figure 19. Trajectory in horizontal planes in different initial states.

Table 6. Perturbation parameters.

Parameters	Perturbations
C_{L_0}	±20%
C_{D_0}	±20%
C_{S_0}	±0.6

1. percentages mean multiplication gain; 2. decimals mean addition value.

The initial state of the Monte Carlo simulation is set as:

- Altitude: 50 m.
- Airspeed: 30 m/s.
- Pitch angle: 0°.
- Roll angle: 0°.
- Radius of landing circle: 268 m.
- Distance to landing point: 680 m.

The simulation results are given in Figures 20–22, where the black lines, blue lines, canyon lines and pinkish red lines mark the fixed-wing flight phase, transitional flight phase, multi-rotors flight phase, and vertical landing phase, respectively, and the red line marks the nominal state result.

Figure 20 shows the three-dimensional trajectory results, where the green circle is the landing circle orbit, the green point is the landing point and canyon point is the landing window. The results show:

- The deceleration and landing process have no altitude surging, and the trajectory is controlled to be narrowly distributed inside the landing circle. The intention to avoid climbing is achieved, and the robust performance of the strategy is excellent.

- The end of the deceleration phase (at the end of the canyon lines) is controlled inside the landing window. Therefore, the strategy ensures a precise landing point, enabling its practical use in vertiport management.

Figures 21 and 22 give the time history of the flight parameters. The results show:

- In the Stage I maneuver (black lines before 8 s), the strategy firstly adjusts the attitudes of the flight to enter a straight-line level flight in fixed-wing mode. This phase has narrowly distributed endings, owing to the fact that the airspeed is fixed until the flight approaches the landing circle.
- In the Stage II maneuver (black lines after 8 s), an abrupt change in the bank angle and pitching angle is observed, owing to the fact that the flight uses the bank maneuver to enter the landing circle orbit and tries to maintain a stable altitude using the pitching angle.
- In the stage III maneuver (blue lines), the attitudes of the aircraft exhibit another abrupt change. During this phase, the guidance logic takes the landing point as the home point to plan a new trajectory, and the flight has to bank to the other side while varying the pitching angle to maintain a stable altitude. Additionally, the hovering rotors are activated in this phase, as shown in Figure 22. The airspeed begins to decline to 20 m/s.
- In the stage IV maneuver (canyon lines), the bank angle settles at -25° and the pitch angle increases monotonically with the decrease in airspeed. During this phase, the lateral attitude is stable, and the partial lift to maintain longitudinal balance is fixed. At mid airspeed, the flight uses the aero-surfaces to provide lift (before 28 s), and then at low airspeed, the hovering rotors are used.
- In the stage V maneuver (pinkish red lines), the altitude decline is obvious, with a low airspeed and wide-ranging angle of attack. During this phase, the flight is landing vertically, and the angle of attack is insignificant, as the flight is thrust-driven.

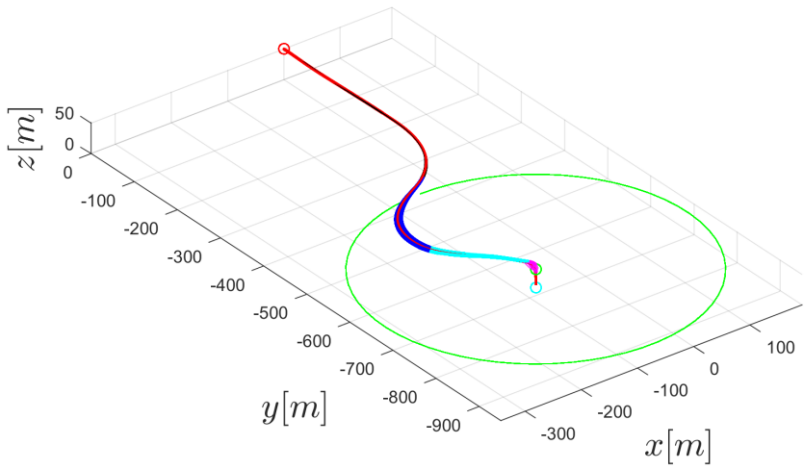

Figure 20. Monte Carlo trajectory results.

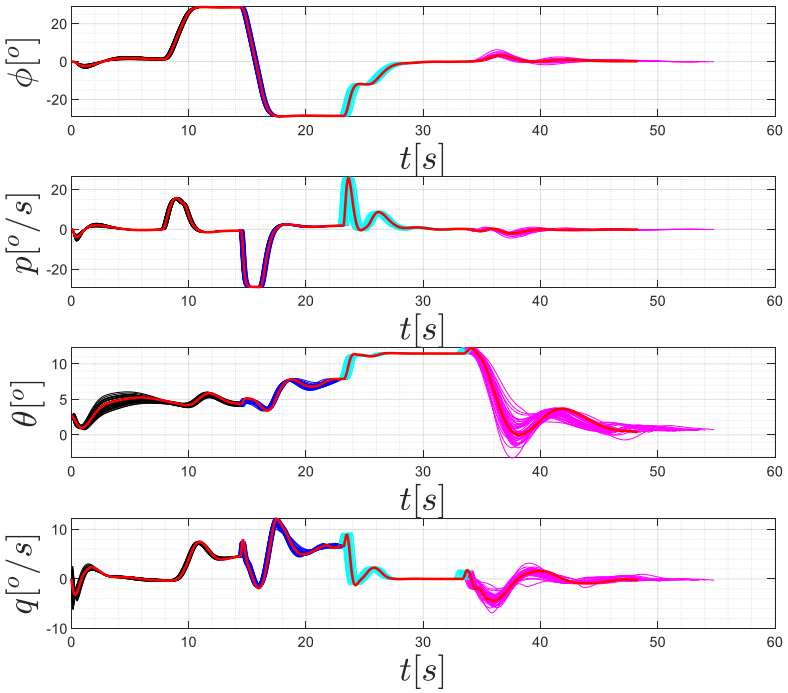

Figure 21. Time histories of longitudinal and lateral flight parameters of the roll-horizon strategy.

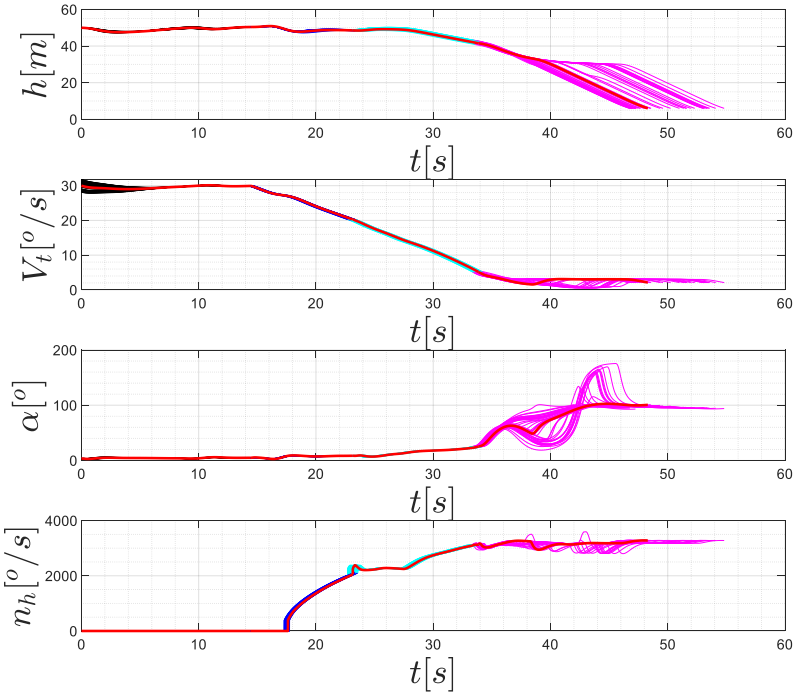

Figure 22. Time histories of altitude, airspeed, angle of attack and rotor speed of the roll-horizon strategy.

5.5. Comparison with Jumping Deceleration and Landing Strategy

The deceleration and landing strategy is proposed to achieve higher efficiency and driving comfort. A comparison with the conventional jumping deceleration strategy, whose trajectory is given in Figure 23, is carried out to verify the energy efficiency.

Figure 24 presents the altitude and velocity channel comparison results. Clearly, the roll-horizon landing strategy has a slight altitude variation, which controls the altitude to within 40 m to 50 m, while the conventional strategy has a large altitude range that covers

40 m to 70 m. In the velocity channel, we found that the time taken to decelerate to 5 m/s (which is the hovering speed) is almost the same (that is, around 19 s), which means the time efficiency for deceleration of the two strategies is equally matched. However, when looking at the slopes of the curves, it can be seen that the slope of the roll-horizon curve is basically unchanged, which indicates a smooth deceleration phase, while the jumping strategy curve has a larger deceleration rate before the altitude inflection point (at about 9 s), which makes the deceleration process less comfortable. In the angle of attack diagram, the conventional jumping strategy has an angle ranging from 0° to 40°, while the roll-horizon strategy angle range is from 0° to 20°, the large angle to 40° is close to the control inability region, which is unacceptable for manned flight.

Figure 25 presents the work and power consumed by the hovering rotors, where P means power and W means work. Obviously, the hovering rotor power of the roll-horizon strategy is lower than that of the jumping strategy throughout the deceleration process. This means a lower workload for the hovering rotors, which is friendly to the rotor life span. Additionally, the lower power means less hovering rotor work, which is depicted more directly in the work diagram. The total work consumed by the roll-horizon strategy is almost half that of the jumping strategy, which is a considerable advantage in terms of energy and economical efficiency.

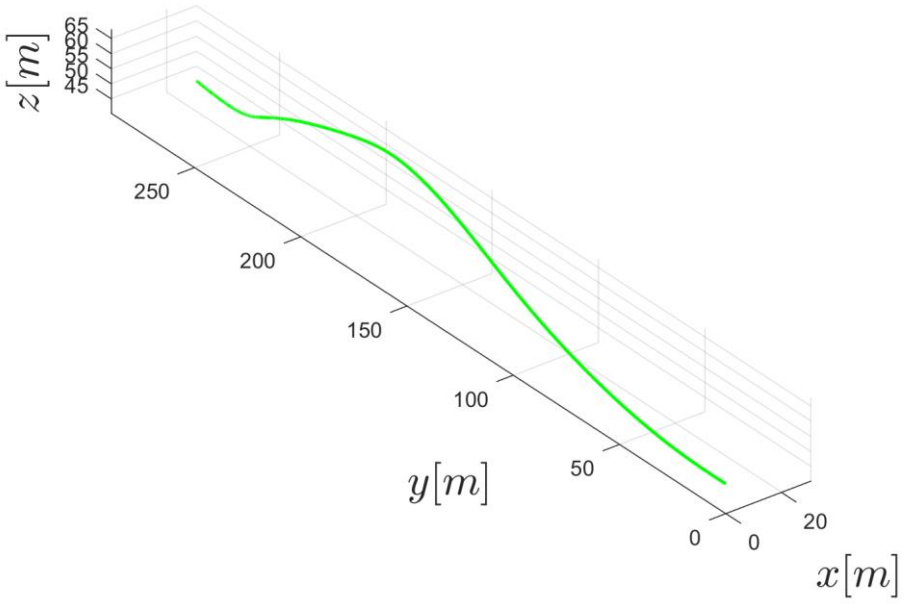

Figure 23. The trajectory of the jumping strategy.

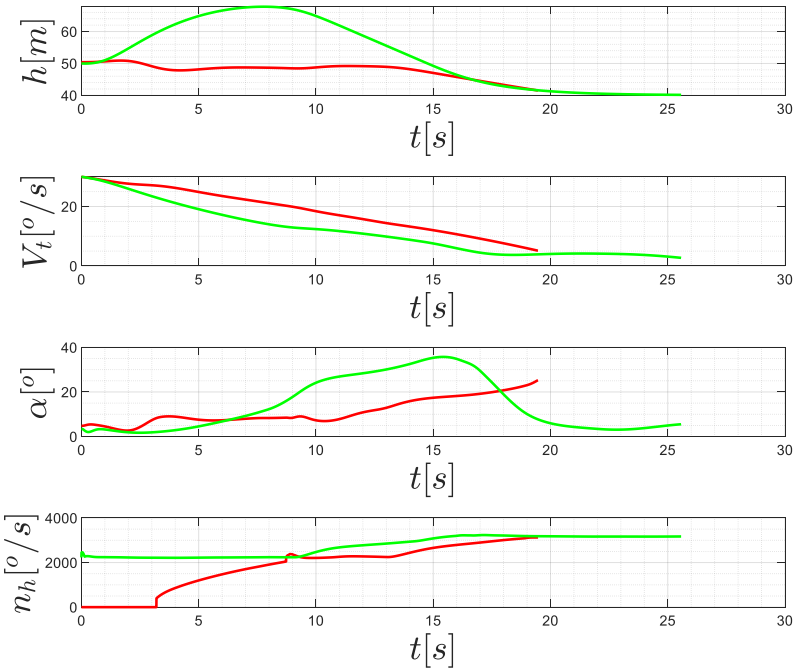

Figure 24. Altitude and velocity channel comparison.

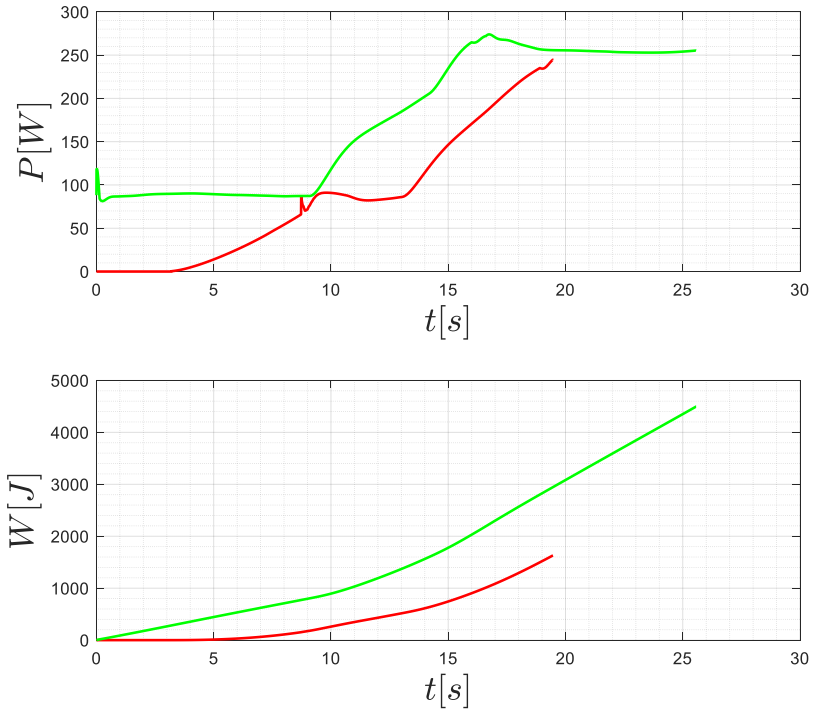

Figure 25. Altitude and velocity channel comparison.

A quantitative comparison is given in Table 7.

Table 7. The comparison results.

Indexes	Roll-Horizon	Jumping
Time to deceleration to 5 m/s	19.4 s	16.5 s
Time to descend to 40 m	19.8 s	21 s
The maximum Altitude	50.67 m	67.8 m
The maximum rotor power	244.7 W	273.9 W
The total rotor work	1613 J	4484 J
The maximum AOA	25.6°	35.65°

It can be found that:

- The time efficiency of the two strategies are similar, where roll-horizon is more efficient at descending while jumping is more efficient at decelerating.
- The roll-horizon strategy successfully avoids climbing during the landing process.
- The power requirement for the hovering rotors of the roll-horizon strategy is less than that of the jumping strategy.
- The total energy consumption of the roll-horizon strategy is less than half that of the jumping strategy.
- The maximum angle of attack of the roll-horizon strategy is lower and appears in the multi-rotor mode.

6. Conclusions

In this work, an L_1 adaptive controller was designed to control the ET120, an eVTOL with complicated flight dynamic characteristics. Furthermore, a roll-horizon deceleration and vertical landing strategy was presented for an improved driving experience and to promote energy efficiency during manned flight. Monte Carlo simulations and comparison simulations were carried out to verify the performance of the control system and the efficiency of the roll-horizon deceleration strategy. The results show that the L_1 adaptive controller-based control system is robust enough to reject at least 20% of perturbation on all modeling parameters. The guidance logic is reliable for completing the maneuvers designed in this strategy and guarantee a safe and bounded deceleration and landing path. The promoted strategy has a smoothly varying airspeed curve, resulting in a more comfortable manned flight, and has a superior energy efficiency, which is able to reduce the hovering rotor work by 64%. Additionally, the strategy avoids dangerous attitudes that may cause the flight to go out of control.

Author Contributions: Conceptualization, Z.W. and S.M.; methodology, Z.W. and Z.G.; software, S.M. and Z.G.; validation, Z.W., S.M. and J.H.; formal analysis, C.Z.; investigation, S.M.; resources, C.Z., J.H. and Z.G.; data curation, S.M.; writing—original draft preparation, S.M.; writing—review and editing, Z.W. and S.M.; visualization, S.M.; supervision, Z.G.; project administration, Z.G.; funding acquisition, Z.G. All authors have read and agreed to the published version of the manuscript.

Funding: This research received no external funding.

Conflicts of Interest: The authors declare no conflict of interest.

References

1. Kim, H.D.; Perry, A.T.; Ansell, P.J. A Review of Distributed Electric Propulsion Concepts for Air Vehicle Technology. In Proceedings of the AIAA/IEEE Electric Aircraft Technologies Symposium, Cincinnati, OH, USA, 9–11 July 2018.
2. Wang, Z.; Zheng., G.; Cheng, Y.; Sun, M.; Xu, J. Practical control implementation of tri-tilt rotor flying wing unmanned aerial vehicles based upon active disturbance rejection control. *Proc. IMechE Part G J. Aerosp. Eng.* **2020**, *234*, 943–960. [CrossRef]
3. Chauhan, S.S.; Martins, J.R.R.A. Tilt-Wing eVTOL Takeoff Trajectory Optimization. *J. Aircr.* **2019**, *57*, 1–20. [CrossRef]
4. Zian, W.; Zheng, G. Longitudinal Flight Characteristics Analysis and Flight Control Design for Hybrid Vtol UAV in Accelerative Transition. *J. Aerosp. Power* **2019**, *34*, 2177–2190.
5. Liu, N.; Cai, Z.; Wang, Y.; Zhao, J. Fast Level-flight to Hover Mode Transition and Altitude Control in Tiltrotor's Landing Operation. *CJA* **2021**, *34*, 181–193. [CrossRef]

6. Daskilewicz, M.; German, B.; Warren, M.; Garrow, L.A.; Boddupalli, S.S.; Douthat, T.H. Progress in Vertiport Placement and Estimating Aircraft Range Requirements for eVTOL Daily Commuting. In Proceedings of the 2018 Aviation Technology, Integration, and Operations Conference, Atlanta, GA, USA, 25–29 June 2018.
7. Yi, L.U.; Zhang, S.; Zhang, Z.; Zhang, X.; Peng, T.A.N.G.; Shan, F.U. Multiple hierarchy risk assessment with hybrid model for safety enhancing of unmanned subscale BWB demonstrator flight test. *Chin. J. Aeronaut.* **2019**, *32*, 2612–2626.
8. Jiang, G.; Liu, G.; Yu, H. A Model Free Adaptive Scheme for Integrated Control of Civil Aircraft Trajectory and Attitude. *Symmetry* **2021**, *13*, 347. [CrossRef]
9. Kleinbekman, I.C.; Mitici, M.; Wei, P. Rolling-horizon Electric Vertical Takeoff and Landing Arrival Scheduling for On-demand Urban Air Mobility. *J. Aerosp. Inf. Syst.* **2020**, *17*, 150–159. [CrossRef]
10. Ayala, V.; Torreblanca, M.; Valdivia, W. Toward Applications of Linear Control Systems on the Real World and Theoretical Challenges. *Symmetry* **2021**, *13*, 167. [CrossRef]
11. Saeed, N.A.; Mahrous Awwad, E.; Abdelhamid, T.; El-Meligy, M.A.; Sharaf, M. Adaptive Versus Conventional Positive Position Feedback Controller to Suppress a Nonlinear System Vibrations. *Symmetry* **2021**, *13*, 255. [CrossRef]
12. Leman, T.; Xargay, E.; Dullerud, G.; Hovakimyan, N.; Wendel, T. L_1 Adaptive Control Augmentation System for the X-48b AircrafAIA Guidance. In Proceedings of the Navigation, and Control Conference, Chicago, IL, USA, 10–13 August 2009; AIAA, Urbana-Champaign: Champaign, IL, USA, 2009.
13. Swarnkar, S.; Parwana, H.; Kothari, M.; Abhishek, A. Biplane-quadrotor Tail-sitter Uav: Flight Dynamics and Control. *J. Guid. Control Dyn.* **2018**, *41*, 1049–1067. [CrossRef]
14. Nigam, N.; Bieniawski, S.; Kroo, I.; Vian, J. Control of Multiple UAVs for Persistent Surveillance: Algorithmand Flight Test Results. *IEEE Trans. Control Syst. Technol.* **2012**, *20*, 1236–1251. [CrossRef]
15. Bordignon, K.; Bessolo, J. Control Allocation for the X-35b. In Proceedings of the 2002 Biennial International Powered Lift Conference and Exhibit, Williamsburg, VA, USA, 5–7 November 2002.
16. Chang, J.; Zhu, J.; Liu, R.; Dong, W. Lateral Control for UItra-low Altitude Airdrop Based on the Ci Adaptive ControlAugmentation. *Int. J. Control Autom. Syst.* **2018**, *16*, 461–477. [CrossRef]
17. Calise, A.J.; Rysdyk, R.T. Nonlinear adaptive flight control using neural networks. *Control Syst. Mag. IEEE* **1998**, *18*, 14–25.
18. Kamel, M.; Burri, M.; Siegwart, R. Linear vs nonlinear MPC for trajectory tracking applied to rotary wing micro aerial vehicles. *IFAC-PapersOnLine* **2017**, *50*, 3463–3469. [CrossRef]
19. Gu, Y.; Seanor, B.; Campa, G.; Napolitano, M.R.; Rowe, L.; Gururajan, S.; Wan, S. Design and Flight Testing Evaluation of Formation Control Laws. *IEEE Trans. Control Syst. Technol.* **2006**, *14*, 1105–1112. [CrossRef]
20. Woodbury, T.; Valasek, J. Synthesis and Flight Test of Automatic Landing Controller Using Quantitative Feedback Theory. *J. Guid. Control Dyn.* **2016**, *39*, 1994–2010. [CrossRef]
21. Xia, X.; Yang, M.; Chen, G.; Zhang, L.; Hou, J. Transition Flight Control and Simulation of a Novel Tail-Sitter UAV With Varying Fuselage Shape. *IEEE Access* **2021**, *99*, 1. [CrossRef]
22. Zou, Y.; Xia, K. Robust Fault-Tolerant Control for Underactuated Takeoff and Landing UAVs. *IEEE Trans. Aerosp. Electron. Syst.* **2020**, *56*, 3545–3555. [CrossRef]
23. Wang, X.; Zhu, B.; Zhu, J.; Cheng, Z. Thrust vectoring control of vertical/short takeoff and landing aircraft. *Sci. China Inf. Sci.* **2020**, *63*, 19–26. [CrossRef]
24. Zou, Y.; Zhang, H.; He, W. Adaptive Coordinated Formation Control of Heterogeneous Vertical Takeoff and Landing UAVs Subject to Parametric Uncertainties. *IEEE Trans. Cybern.* **2020**, *99*, 1–12. [CrossRef]
25. Betancourt, J.; Castillo, P.; Lozano, R. Stabilization and Tracking Control Algorithms for VTOL Aircraft: Theoretical and Practical Overview. *J. Intell. Robot. Syst.* **2020**, *100*, 1249–1263. [CrossRef]
26. Vajpayee, V.; Becerra, V.; Bausch, N.; Deng, J.; Shimjith, S.R.; Arul, A.J. L1-Adaptive Robust Control Design for a Pressurized Water-type Nuclear Power Plant. *IEEE Trans. Nucl. Sci.* **2021**, *68*, 1381–1398. [CrossRef]
27. Zhao, J.; He, X.; Li, H.; Lu, L. An adaptive optimization algorithm based on clustering analysis for return multi-flight-phase of VTVL reusable launch vehicle. *Acta Astronaut.* **2021**, *183*, 112–125. [CrossRef]
28. Cao, C.; Hovakimyan, N. Design and Analysis of a Novel L1 Adaptive Controller, Part I: Control Signal and Asymptotic Stability. In Proceedings of the 2006 American Control Conference, Minneapolis, MN, USA, 14–16 June 2006; IEEE: Los Alamitos, CA, USA, 2006.
29. Cao, C.; Hovakimyan, N. Design and Analysis of a Novel L1 Adaptive Controller, Part II: Guaranteed. In Proceedings of the Transient Performance. 2006 American Control Conference, Minneapolis, MN, USA, 14–16 June 2006; IEEE: Los Alamitos, CA, USA, 2006.
30. Xargay, E.; Hovakimyan, N.; Dobrokhodov, V.; Statnikov, R.; Kaminer, I.; Cao, C.; Gregory, I. L_1 Adaptive Flight Control System: Systematic Design and Verification and Validation of Control Metrics. In Proceedings of the AIAA Guidance, Navigation, and Control Conference, Toronto, ON, Canada, 2–5 August 2010.
31. Wise, K.; Lavretsky, E.; Hovakimyan, N.; Cao, C.; Wang, J. Verifiable Adaptive Flight Control. In Proceedings of the AIAA Guidance, Navigation, and Control Conference, San Francisco, CA, USA, 15–18 August 2005.